Energy considerations in the SPH method with deformable boundaries and application to FSI problems

C. Hermange, G. Oger, D. Le Touzé

Contents lists available at ScienceDirect

Journal of Computational Physics

journal homepage: www.elsevier.com/locate/jcp

Energy considerations in the SPH method with deformable boundaries and application to FSI problems

C. Hermange[a,b,*], G. Oger[b], D. Le Touzé[b]

[a]*La Manufacture Franaise des Pneumatiques MICHELIN, Clermont-Ferrand, France*
[b]*Ecoel Centrale Nantes, LHEEA Lab. (ECN/CNRS), Nantes, France*

ARTICLE INFO

Article history:
Received 1 May 2013
Received in final form 10 May 2013
Accepted 13 May 2013
Available online 15 May 2013

Communicated by S. Sarkar

Keywords: SPH-FE Coupling, Fluid-structure interaction, Energy conservation, Interface coupling energy

ABSTRACT

This study aims at improving a coupling strategy between Smoothed Particle Hydrodynamics (SPH) with Finite Element (FE) methods in order to model violent Fluid-Structure Interaction (FSI) problems. An analysis of the SPH-FE coupling from the energetic point of view is carried out. The purpose of this work is to quantify the loss/gain in energy at the fluid-structure interface, within the fluid, and within the structure. Interface energy is especially compared to other energy components, highlighting the importance of this term. Different structure models are considered. Additionally, few proposals are made for improving the quality and efficiency of the coupling strategy. Investigations are performed on 2D simulations of both academic and experimental test cases.

1. Introduction

Coupled fluid-structure interaction effects need to be predicted and possibly mitigated in a wide range of applications: aerospace, nuclear and ocean engineering, biomechanics, car industry. Different methods have been developed in order to model coupled phenomena for which strong reciprocal effects occur. The present paper focuses on SPH-FE coupling strategy to model violent fluid-structure interactions involving complex free surface flows with deformable structures. On the solid side, a classical FE method [6] is used. On the fluid side, the SPH method is used to easily consider complex free surface flows. This method has been introduced at the end of the 70's by Gingold and Monaghan [18] and Lucy [28]. The meshless and Lagrangian features of SPH naturally solve the problem of fluid/solid grid compatibility. Neither contact algorithms between fluid and solid nor free surface tracking are needed. This property results in a significantly reduced complexity of the fluid-structure interface treatment. Another advantage of SPH resides in its compressible feature, allowing for considering actual compressible effects when needed and also permitting the incompressible fluid assumption (weakly-compressible approach). Note also that this coupling strategy leads to a purely Lagrangian description in both media.

*Corresponding author:
e-mail: corentin.hermange@ec-nantes.com (C. Hermange)

Various SPH-FE coupling methods have already been proposed since the 90's (see for instance Johnson [21] and Attaway *et al.* [5]). Most popular strategies are based on a master-slave coupling, in which contact forces are used to couple SPH particles and Finite Element meshes [19, 45, 8]. Each method has its own specificity (see for instance [12] where FE nodes are considered as SPH particles). Fourey *et al.* [16, 17], Yang *et al.* [43, 44] and more recently Li *et al.* [23, 25] showed the interest of SPH-FE coupling for complex FSI problem modelling without contact algorithms. Nevertheless some problems still persist. Coupling methods need to be improved regarding the computation speed [32], but also regarding the robustness [17]. Indeed, high frequency fluid loads tend to destabilize the solution. Therefore, sufficient dissipation of high frequencies should be added in the structure to stabilize the coupling. Furthermore some improvements are needed to build more robust strategies regarding a better load transfer from the fluid to the solid.

In this work, we analyse an SPH-FE coupling method from the energetic point of view. According to Farhat and Lesoinne [15] and Piperno *et al.* [37, 38] energy conservation and information transfers are primordial for coupling performances, accuracy and stability. In their work on coupling algorithms, Michler *et al.* and Degroote *et al.* [31, 13] underlined that partitioned algorithms do not permit the exact satisfaction of interface conditions, contrary to monolithic schemes. Any fluid-structure interaction model displays losses or gains of energy at the interface between fluid and deformable body. In their work, Li *et al.* [23, 24, 25] proposed a coupling strategy imposing an energy conservation at the interface. Conversely, Fourey *et al.* [16, 17] did not impose such a condition but succeeded in obtaining satisfactory results. Li *et al.* [25] did not make a coupling energy estimation analysis. We consider that energy losses or gains should still be estimated in respect to other dissipative energies, to better understand the importance of enforcing conservation at the interface. Ensuring the rightful energy exchanges between the solid and the fluid is fundamental to build a correct model for fluid-structure interactions. Therefore the energy conservation properties of our SPH-FE coupling strategy are investigated. We first quantify the interface energy by following the same process as the one in Antuono *et al.* [4]. Interface coupling energy is then compared to other energy components, especially with the numerical dissipation due to the stabilization of the SPH scheme and with the total fluid energy. Influence of various coupling parameters are also investigated. Finally various techniques for the determination of pressure loads on the deformable body are proposed and discussed.

This paper is organized as follows : section 2 presents energy considerations for SPH-FE coupling strategies. It also provides a definition of the interface coupling energy. Then section 3 introduces an energy balance for SPH models. In section 4 an energetic analysis of our present coupling strategy is performed on an academic test case from Scolan [40] and an experimental one from Antoci [1]. Then section 5 proposes some improvements of the SPH-FE coupling strategy proposed, through a new loading method. Numerical results are discussed in terms of robustness and efficiency.

2. Energy considerations for SPH-FE coupling strategy

The discussion revolves around the coupling strategy adopted by Fourey *et al.* [17]. Classical partitioned approaches are used, aiming at developing a coupling strategy that is robust and compatible with any kind of SPH and FE solvers.

2.1. Coupling strategy

The deformable body is modelled using the open-source generalist software **Code_Aster** developed by EDF (www.code-aster.org). The fluid part is modelled using the SPH-flow solver, jointly developed by the LHEEA Lab. of Ecole Centrale Nantes and NEXTFLOW Software [36, 35]. As illustrated in Fig. (1), both SPH and FE solvers are considered as black boxes exchanging fluid pressure loads and structure node positions and velocities with a dedicated third program (coupling program) responsible for managing the data exchanges needed (MPI communications). This strategy eases the interchangeability of solvers and avoid any specific hard-coding. As a result, and contrary to Li *et al.* [24] or Yang *et al.* [43, 44] for instance, each solver can be easily modified and improved independently from each other.

2.2. Treatment of deformable bodies

From the SPH algorithmic point of view, a deformable body at instant t is considered as a rigid wall, but with specific local deformation velocities (and node positions) provided by the FE solver. It is possible to choose any boundary method, ghost particle method [26, 10] or NFM [29, 30, 11]. No other treatment is prescribed to treat the

deformable body interface. Especially, no contact algorithm dedicated to avoid material interpenetration is therefore needed, contrary to [19] for instance. As proposed in [34], the pressure loads P_k applied to each FE structure mesh is computed using the SPH fluid pressure solution averaged from the near face boundary area. More precisely, pressure loads are defined as an average of all particles seen by the wet body panel (Fig. (2)) within a distance R from the panel, where R is the kernel radius used is the SPH spatial operators:

$$P_k = \frac{1}{N_a} \sum_{i=1}^{N_a} P_i, \tag{1}$$

where N_a is the number of particles within the averaging area.

The average pressure area is chosen as proportional to R for spatial convergence purposes, since R is a convergence measure in the SPH method. As emphasized in [34], pressure averaging tends to smooth the irregularities near the wet body panel, which is important in the present work as pressure load irregularities may be responsible for coupling instabilities. A sufficient number of particles is necessary for each panel, of which the size has to be adapted in order to capture the physical load variations. The influence of the number of particles per panel onto the coupling robustness will not be investigated here, but it could be the purpose of a future work.

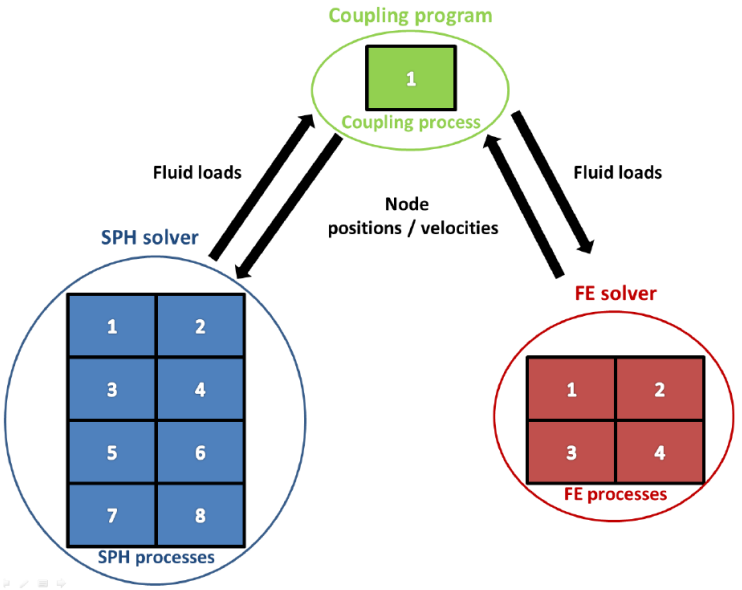

Fig. 1. SPH-FE coupling strategy. Example involving 8 cores and 4 cores respectively for SPH and FE solvers. A single core is dedicated to the coupling management (coupling program).

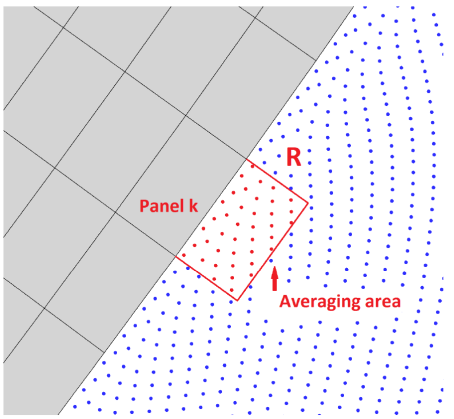

Fig. 2. Averaged pressure calculation on a wet body panel k.

2.3. Coupling algorithm

A *Conventional Parallel Staggered* (CPS) procedure is used in this study (see Fig. (3)). The scheme is described in Farhat *et al.* [15] for mesh-based methods. The CPS algorithm has been shown to be less stable than a classical sequential procedure [17]. The alternating operation of a sequential algorithm introduces a shift of the solution to improve the stability. The sequential procedure also corresponds to the algorithm that best fits with the implicit nature of the FE solver. Indeed the CPS algorithm makes the assumptions that the fluid loading $F_{fluid/body}$ does not vary between two instants (i.e. $F^{n+1}_{fluid/body} \approx F^{n}_{fluid/body}$). Such an approximation is acceptable since the weakly compressible approach imposes very small time steps. Furthermore a parallel procedure mitigates the CPU costs. The computation time of fluid and solid solvers are overlapped by a synchronous updating (i.e. are not added together).

To maintain the coupling stability using parallel procedures Fourey *et al.* [17] propose to add some diffusion in the FE time integration scheme. Here we focus on two classical implicit schemes, Newmark and Hilber-Hughes-Taylor (HHT) [20]. The latter one is less diffusive but it reduces high frequency oscillations without affecting the low

frequency domain. In both schemes the diffusion is controlled by a parameter $\alpha_s \in [-0.3, 0]$, $\alpha_s = -0.3$ corresponding to the maximal diffusion. The numerical diffusion is actually needed to stabilized the solution when the structure is subjected to high frequency loads. This is particularly relevant for coupling with the SPH method which is usually responsible for acoustic pressure waves due to its weakly-compressible nature, which can affect the coupling stability.

In practice the time step is the same for fluid and solid solvers. As the maximum fluid time step allowed is expected to be smaller than the solid one, *SPH-Flow* imposes its time steps to *Code_Aster*. This condition is always satisfied using an explicit resolution in the fluid and an implicit one in the solid. The fluid solver sends its time step value and pressure loads to the FE solver and receives the body node positions and velocities. Each solver then simultaneously evolves from t^n to t^{n+1}.

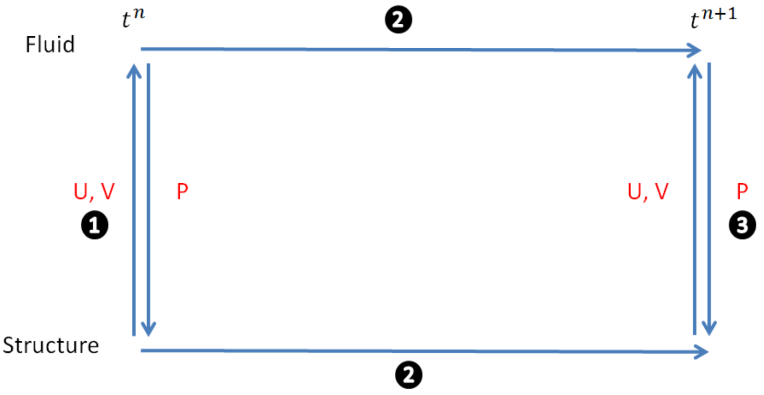

Fig. 3. CPS coupling algorithm

Recently Li *et al.* [24] proposed a specific coupling strategy enforcing energy conservation at the interface. This technique is strongly intricated with the FE model, and therefore implies hard-coding within the solid solver. Conversely, the weak-coupling strategy retained in this study is flexible, easy to implement and compatible with any kind of SPH schemes and boundary condition treatment. The solid solver is considered as a "black box" receiving fluid loads and returning updated solid positions and velocities, so that any FE software can actually be used. No additional CPU time is introduced as no interface treatment is required.

2.4. Coupling algorithm

Antuono *et al.* proposed a study related to energy conservation in the SPH method [4], in the absence of solid bodies and for the δ-SPH scheme. Their work analyses the contribution of this term from the continuity equation, highlighting that the diffusive term is generally small and linked to the excitation of spurious high-frequency acoustic waves. Then Cercos-Pita *et al.* [9] performed this investigation in presence of rigid body interactions, highlighting that imposing boundary conditions using ghost particles introduces some extra-terms in the energy equations. These extra-terms are actually related to the fluid-structure interactions.

Here energy conservation properties are analysed by considering the case of a fluid interacting with a deformable body through SPH-FE coupling. The energy terms are expressed for two SPH schemes, with a particular focus on internal and boundary energies. The analysis start with the δ-SPH method [3, 4], before making its analogy with the Riemann-SPH [41, 22] scheme actually used throughout this paper. An energy balance over the entire domain is considered (fluid + solid), as the global domain must ensure the conservation of energy (Fig. (4)). In the absence of outer contributions, several sources of energy creation or dissipation exist. The first source comes from the inside of each sub-domain. It corresponds to numerical diffusions and can be expressed as an internal irreversible energy. The second source of dissipation / creation comes from the treatment of the fluid structure interface.

Determining the numerical diffusion in the SPH method is relatively straightforward, contrary to the FE method which requires to compare the energy at time t to its initial value. Note that the numerical diffusion in each subdomain is negligible in comparison with other terms (at least for sufficiently converged solutions in these cases). In the following simulations, the numerical diffusion within the fluid is expected to be higher than within the solid. Indeed conservation properties are significantly better in the FE method than in the SPH one.

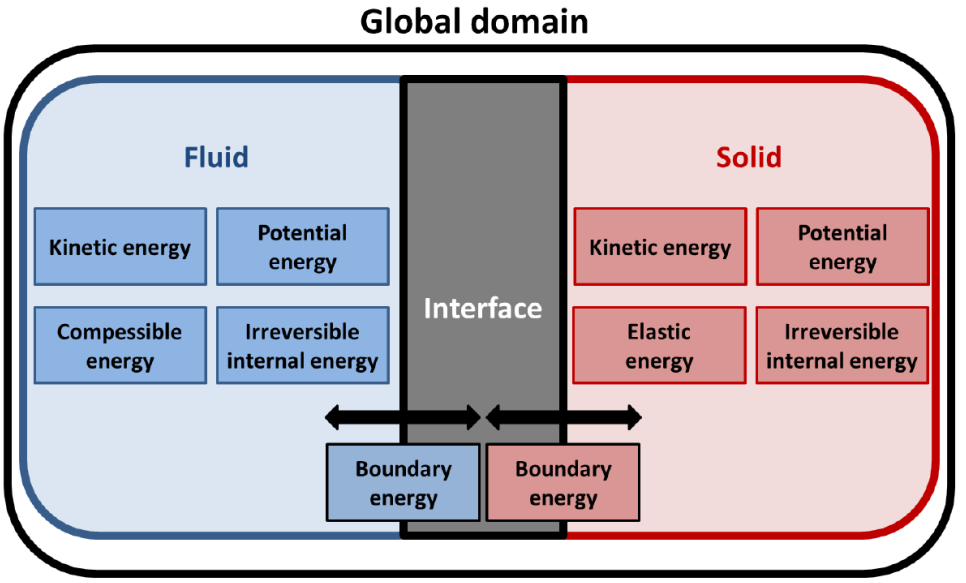

Fig. 4. Energy balance over the global domain

The second source of dissipation/creation is more subtle, as emphasized in this work. From the FE point of view the interface definition is quite obvious, as it corresponds to the wet surface of the deformable solid (Fig. (5)) that is loaded with the fluid pressure. The energy $mathcalE_{fluid/body}$ transferred at the interface follows:

$$\frac{d\mathcal{E}_{fluid/body}}{dt} = -\sum_{k\in B} P_k S_k \vec{n_k}.\vec{V_k}, \tag{2}$$

where B is the set of wet faces of surface S_k, $\vec{n_k}$ the local normal, $\vec{v_k}$ the local velocity and P_k is the fluid pressure applied on S_k (Fig. (2)).

However, to define the exact location of the interface is not obvious from the SPH method point of view. In a first approach, one can consider that it coincides with the wet surface (i.e. with the FE faces). Under this assumption the energy transmitted at the interface could be the same from SPH ($\mathcal{E}_{body/fluid}$) and FE ($\mathcal{E}_{fluid/body}$) point of views. Nevertheless, the spatial operators of SPH make that the deformable body does not coincide exactly with the area of application of solid forces on the fluid. This area is located in the near boundary region (Fig. (5)). In a second approach (more Hamiltonian) the interface could be considered as the whole set of particles contributing to solid boundary conditions (i.e. the particles having a support kernel truncated by a FE face). It is then possible to compute the power actually transmitted from the deformable solid to each fluid particle.

The fluid-structure interface treatment is therefore quite subtle as the energy transmitted through the interface should be computed on different locations. Moreover this energy does not depend exclusively on pressure forces but also on other fluid characteristics as discussed further. At convergence the SPH and FE interface energies should tend to be the same:

$$\mathcal{E}_{body/fuid} \approx \mathcal{E}_{fluid/body}, \tag{3}$$

otherwise an interface coupling energy $\mathcal{E}_{Interface}$ can be defined as:

$$\mathcal{E}_{Interface} = \mathcal{E}_{body/fuid} - \mathcal{E}_{fluid/body}. \tag{4}$$

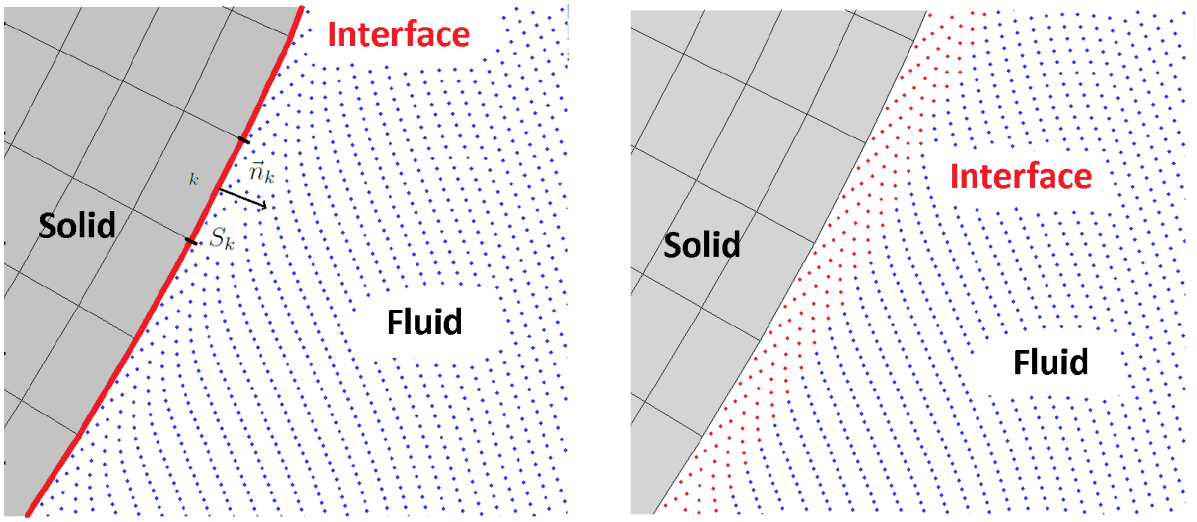

Fig. 5. Fluid-structure interface from the solid (left) and fluid (right) point of views.

3. Energy balance in δ-SPH and Riemann-SPH schemes

A weakly-compressible and inviscid fluid is considered in this study. Navier-Stokes equations are therefore reduced to the following Euler equations (written in a moving Lagrangian referential):

$$\frac{d\vec{x}}{dt} = \vec{v}, \tag{5}$$

$$\frac{d\rho}{dt} = -\rho\vec{\nabla}.\vec{v}, \tag{6}$$

$$\frac{d\vec{v}}{dt} = \vec{g} - \frac{\vec{\nabla}P}{\rho}, \tag{7}$$

where $\vec{x}$, $\vec{v}$, ρ and P are respectively the position, velocity, density and pressure. This system is closed using the following equation of state:

$$P = \frac{\rho_0 C_0^2}{7}\left[\left(\frac{\rho}{\rho_0}\right)^7 - 1\right], \tag{8}$$

where ρ_0 and C_0 are respectively the reference density and speed of sound.

The time advance is performed explicitly using a 4^{th} Runge-Kutta scheme. The time step should therefore respect the following CFL condition:

$$\Delta t < CFL\frac{R}{C_o}, \tag{9}$$

where R is the kernel radius and CFL is the Courant number taken as $CFL = 0.375$. This feature leads classically to very small time steps. For cases involving violent fluid-structure interaction problems, we usually expect the fluid time step to remain smaller than the solid one.

The energy balance for two SPH schemes is provided in this section, with emphasis on irreversible internal and boundary energies. The contributions of each energy term will be expressed independently of each other. We start with the *delta*-SPH method, before its analogy with a Riemann-SPH scheme which is then used throughout this study. This section proposes a methodology to estimate all energy components using the discrete equations. The total energy can be expressed as the sum of three terms: potential, kinetic and internal energies.

$$\mathcal{E}_{TOT} = \mathcal{E}_P + \mathcal{E}_K + \mathcal{E}_I. \tag{10}$$

3.1. δ-SPH scheme

The SPH method discretises the fluid with a set of particles. As proposed by Antuono *et al.* [3], the set of discrete equations for a particle i is defined as:

$$\frac{d\vec{x_i}}{dt} = \vec{v_i}, \tag{11}$$

$$\frac{d\rho_i}{dt} = -\rho_i \sum_{j=1}^{N} (\vec{v_j} - \vec{v_i}).\vec{\nabla}_i W_{ij}\omega_j + \sum_{j=1}^{N} \vec{\psi_{ij}}.\vec{\nabla}_i W_{ij}\omega_j, \tag{12}$$

$$\rho_i \frac{d\vec{v_i}}{dt} = \rho_i \vec{f_i} - \sum_{j=1}^{N} (P_i + P_j)\vec{\nabla}_i W_{ij}\omega_j + \sum_{j=1}^{N} \Pi_{ij}\vec{\nabla}_i W_{ij}\omega_j, \tag{13}$$

with

$$\Pi_{ij} = \alpha_\delta h C_0 \rho_0 \frac{\vec{x_{ij}}.\vec{v_{ij}}}{\left\|\vec{x_{ij}}\right\|^2} \text{ and } \vec{\psi}_{ij} = 2\delta_\delta h C_0 \left[(\rho_j - \rho_i) - \frac{1}{2}(\vec{\nabla}^{RL}\rho_i + \vec{\nabla}^{RL}\rho_j).\vec{x_{ij}}\right] \frac{\vec{x_{ij}}}{\left\|\vec{x_{ij}}\right\|^2}, \tag{14}$$

where ρ_i,ω_i,$\vec{x_i}$ and $\vec{v_i}$ are respectively the density, volume, position and velocity of the particle i. Here $\vec{x_{ij}} = \vec{x_i} - \vec{x_j}$ and $\vec{v_{ij}} = \vec{v_i} - \vec{v_j}$. Furthermore coefficients δ_δ and α_δ control the order of magnitude of the diffusive and viscous terms respectively. W is a Wendland kernel function [42], h the smoothing length and N represents the number of neighbour particles in the compact support of W.$\vec{\nabla}^{RL}$ is the renormalized gradient operator [39]. Here the only volumic force is the gravity: $\vec{f_i} = \vec{g_i}$.

Free-slip boundary conditions are considered throughout this study. Effects of structure deformations onto the fluid are imposed through the boundary conditions exclusively, so that they represent a key point in the proposed coupling strategy. Boundary conditions are imposed through the use of ghost particles [26, 10]. These particles are used to complete the kernel support of a particle located near a boundary, in order to enforce the kinematic and dynamic boundary conditions. Theoretically, the ghost particle pressure should take into account the local body acceleration [7**?**]:

$$\frac{\partial P}{\partial n} = \rho\left(\frac{d\vec{V}_{wall}}{dt}.\vec{n} - \vec{g}.\vec{n} + (\vec{V}_{wall} - \vec{V}).\frac{dn}{dt}\right), \tag{15}$$

where $\vec{n}$ and $\vec{V}_{wall}$ are respectively the local normal and the velocity of the wall. Nevertheless for the following applications considered in this work, we suppose that the contributions $\frac{d\vec{V}_{wall}}{dt}.\vec{n}$ and $(\vec{V}_{wall} - \vec{V})\frac{dn}{dt}$ are negligible compared to other components. As a result, the ghost particle pressure $P_{G(i)}$ and velocity $\vec{v}_{G(i)}$ are defined as:

$$P_{G(i)} = P_i - \rho_i(\vec{g}_i.\vec{n})\left[(\vec{x}_i - \vec{x}_{G(i)}).\vec{n}\right], \tag{16}$$

$$\vec{v}_{G(i)} = \vec{v}_i + 2(\vec{V}_{wall}.\vec{n} - \vec{V}_i.\vec{n})\vec{n}. \tag{17}$$

For complex geometries, the creation of ghost particles is not straightforward and results in a possibly large algorithmic complexity. We refer the reader to [33] for more details on this particular point.

3.1.1. Potential energy

The variation of potential energy is classically defined as:

$$\frac{d\mathcal{E}_P}{dt} = -\sum_{i=1}^{N_{FP}} \rho_i \omega_i \vec{v}_i.\vec{g}_i, \tag{18}$$

where N_{FP} is the total number of particles in the fluid domain.

3.1.2. Kinetic energy

The variation of kinetic energy per unit mass $\mathcal{E}_K^m$ is expressed as:

$$\rho\frac{d\mathcal{E}_K^m}{dt} = \rho\vec{V}.\vec{g} - \vec{V}\vec{grad}P + \vec{V}.\vec{div}\overline{\overline{\tau}}. \tag{19}$$

The right hand side terms in Eq. (19) correspond respectively to the power of volumetric forces, the power of pressure forces and the power of viscous constraints. In this study an inviscid fluid is considered (i.e. $\overline{\overline{\tau}} = 0$). The variation of internal energy per unit mass therefore writes:

$$\rho\frac{d\mathcal{E}_K^m}{dt} = \rho\vec{V}.\vec{g} - \vec{V}\vec{grad}P. \tag{20}$$

The δ-SPH scheme assumes a constant mass for each particle i (i.e. $\frac{dm_i}{dt} = 0$) with $m_i = \omega_i\rho_i$. In these conditions the variation of global kinetic energy within the whole domain writes:

$$\frac{d\mathcal{E}_K}{dt} = \sum_{i=1}^{N_{FP}}\rho_i\omega_i\vec{v_i}.\vec{g_i} - \sum_{i=1}^{N_{FP}}\sum_{j=1}^{N}(P_i + P_j)\vec{v_i}.\vec{\nabla}_i W_{ij}\omega_i\omega_j + \sum_{i=1}^{N_{FP}}\sum_{j=1}^{N}\Pi_{ij}\vec{v_i}.\vec{\nabla}_i W_{ij}\omega_i\omega_j, \tag{21}$$

where the artificial viscosity is considered as a pressure-like term $\Pi_i = \frac{\Pi_{ij}}{2}$. Note that this equation can directly be obtained by multiplying the momentum equation by the velocity and then by summing over the fluid particles.

3.1.3. Internal energy

The variation of internal energy per unit mass $\mathcal{E}_I^m$ is expressed as:

$$\frac{d\mathcal{E}_I^M}{dt} = -P\mathrm{div}\vec{V} + \overline{\overline{\tau}} : \overline{\overline{D}} + r - \mathrm{div}\vec{Q}. \tag{22}$$

where r is a heat source, $\vec{Q}$ a heat surface flux, $\overline{\overline{\tau}} : \overline{\overline{D}}$ the viscous dissipation, and $-Pdiv\vec{V}$ a compressible power. In this study both r and $\vec{Q}$ are assumed to be zero, and an inviscid fluid is considered ($\overline{\overline{\tau}} : \overline{\overline{D}} = 0$). The variation of internal energy within the whole domain therefore writes:

$$\frac{d\mathcal{E}_I}{dt} = -\sum_{i=1}^{N_{FP}}\sum_{j=1}^{N}P_i(\vec{v}_j - \vec{v}_i).\vec{\nabla}_i W_{ij}\omega_i\omega_j + \sum_{i=1}^{N_{FP}}\sum_{j=1}^{N}\Pi_{ij}(\vec{v}_j - \vec{v}_i).\vec{\nabla}_i W_{ij}\omega_i\omega_j. \tag{23}$$

Let us focus on the first term of Eq. (23). Following [4] it is possible to distinguish two parts:

$$-\sum_{i=1}^{N_{FP}}\sum_{j=1}^{N}P_i(\vec{v}_j - \vec{v}_i).\vec{\nabla}_i W_{ij}\omega_i\omega_j = \underbrace{\sum_{i=1}^{N_{FP}}\frac{\omega_i}{\rho_i}P_i\frac{d\rho_i}{dt}}_{\frac{d\mathcal{E}_C}{dt}} - \underbrace{\sum_{i=1}^{N_{FP}}\sum_{j=1}^{N}\frac{P_i}{\rho_i}\vec{\psi}_{ij}.\vec{\nabla}_i W_{ij}\omega_i\omega_j}_{\mathcal{P}_\delta}, \tag{24}$$

where $\mathcal{P}_\delta$ represents the power associated to the diffusive term in the mass conservation equation:

$$\mathcal{P}_\delta = \sum_{i=1}^{N_{FP}}\sum_{j=1}^{N}\frac{P_i}{\rho_i}\vec{\psi}_{ij}.\vec{\nabla}_i W_{ij}\omega_i\omega_j, \tag{25}$$

and $\mathcal{E}_C$ is a reversible compressible energy due to the compressible feature of the SPH method:

$$\frac{d\mathcal{E}_C}{dt} = \sum_{i=1}^{N_{FP}}\frac{\omega_i}{\rho_i}P_i\frac{d\rho_i}{dt}, \tag{26}$$

however in a weakly-compressible SPH method this energy is expected to remain rather small.

It is now possible to express the internal energy into two parts $\mathcal{E}_I = \mathcal{E}_C + \mathcal{E}_V$ as:

$$\frac{d\mathcal{E}_V}{dt} = -\mathcal{P}_\delta + \sum_{i=1}^{N_{FP}}\sum_{j=1}^{N}\frac{\Pi_{ij}}{2}(\vec{v}_j - \vec{v}_i).\vec{\nabla}_i W_{ij}\omega_i\omega_j. \tag{27}$$

$\mathcal{E}_V$ is an irreversible internal energy. It represents the energy lost to stabilize the SPH method. It does not affect the consistency of the SPH scheme since it tends to vanish as the spatial resolution increases.

3.1.4. Boundary energy

Considering solid boundaries, a certain amount of energy can be lost or gained by the fluid. This energy is called $\mathcal{E}_{body/fluid}$. Using the ghost particle method, [10], the variation of the total energy verifies:

$$\frac{d\mathcal{E}_{TOT}}{dt} = \frac{d(\mathcal{E}_P + \mathcal{E}_K + \mathcal{E}_C + \mathcal{E}_V)}{dt} = \frac{d\mathcal{E}_{body/fluid}}{dt}, \tag{28}$$

so that

$$\begin{aligned}
\frac{d\mathcal{E}_{body/fluid}}{dt} &= -\sum_{i=1}^{N_{FP}}\sum_{j=1}^{N_g}(P_i + P_j)\vec{v}_i.\vec{\nabla}_i W_{ij}\omega_i\omega_j + \sum_{i=1}^{N_{FP}}\sum_{j=1}^{N_g}\Pi_{ij}\vec{v}_i.\vec{\nabla}_i W_{ij}\omega_i\omega_j \\
&\quad -\sum_{i=1}^{N_{FP}}\sum_{j=1}^{N_g}P_i(\vec{v}_j - \vec{v}_i).\vec{\nabla}_i W_{ij}\omega_i\omega_j + \sum_{i=1}^{N_{FP}}\sum_{j=1}^{N_g}\frac{\Pi_{ij}}{2}(\vec{v}_j - \vec{v}_i).\vec{\nabla}_i W_{ij}\omega_i\omega_j \\
&= -\sum_{i=1}^{N_{FP}}\sum_{j=1}^{N_g}(P_i\vec{v}_j + P_j\vec{v}_i).\vec{\nabla}_i W_{ij}\omega_i\omega_j + \sum_{i=1}^{N_{FP}}\sum_{j=1}^{N_g}\frac{\Pi_{ij}}{2}(\vec{v}_j + \vec{v}_i).\vec{\nabla}_i W_{ij}\omega_i\omega_j,
\end{aligned} \tag{29}$$

where N_g is the number of ghost particles inside the kernel support.

Note that the wall velocity does not directly appear in this formulation: it is included within the ghost velocity $\vec{v}_j$ Using this approach, the transfer of energy from the solid to the fluid is estimated using all fluid particles having a truncated kernel near the boundary. Furthermore, nothing formally imposes $\frac{d\mathcal{E}_{body/fluid}}{dt}$ and $\frac{d\mathcal{E}_{fluid/body}}{dt}$ to be equal. There is indeed no direct correlation between Eq. (29) and Eq. (2). One can only expect that these two quantities are as close as possible. Furthermore considering fixed and flat boundaries without gravity leads to $\mathcal{E}_{body/fluid} = 0$. Indeed ghost particles have the same pressure as their mother particles, and an opposite normal velocity. The conservation of the total energy is therefore ensured: $\frac{d\mathcal{E}_{TOT}}{dt} = 0$.

3.1.5. Summary

The energy components of the δ-SPH scheme have been presented separately in detail, highlighting the presence of a boundary term which represents the power yielded or received through the solid boundaries. Different dissipative contributions which take part in increasing the irreversible internal energy have also been outlined. This dissipative energy is critical for the stability of SPH simulations.

3.2. Riemann-SPH scheme

The simulations discussed in the next sections are performed using a Riemann-SPH scheme [41]. Here, the formulation proposed by Leduc *et al.* [22] is used, ensuring the local mass conservation. We show here that this scheme is very close to the δ-SPH one. The Riemann scheme considered is defined by the following system:

$$\frac{d\vec{x_i}}{dt} = \vec{v_i}, \tag{30}$$

$$\frac{d\rho_i}{dt} = \omega_i\sum_{j=1}^{N}2(\vec{v_e} - \vec{v_i}).\vec{\nabla}_i W_{ij}\omega_j, \tag{31}$$

$$\frac{dm_i}{dt} = 0, \tag{32}$$

$$\frac{dm_i\vec{v_i}}{dt} = \omega_i\rho_i\vec{g} - \sum_{j=1}^{N}2P_e\vec{\nabla}_i W_{ij}\omega_i\omega_j, \tag{33}$$

where $\mathcal{P}_e$ and $\vec{v}_e$ are the linearized Riemann problem solutions. Eq. (32) leads to:

$$\frac{d\rho_i}{dt} = -\frac{\rho_i}{\omega_i}\frac{d\omega_i}{dt} = -\sum_{j=1}^{N}2\rho_i(\vec{v_e} - \vec{v_i})\vec{\nabla}_i W_{ij}\omega_j. \tag{34}$$

These mass and momentum conservation equations are very similar to the ones in δ-SPH scheme Eq. (12) and Eq. (13). Using:

$$\vec{\psi}'_{ij} = -\rho_i(2\vec{v_e} - \vec{v_i} - \vec{v_j}), \tag{35}$$

$$\Pi'_{ij} = (P_i + P_j - 2P_e), \tag{36}$$

the mass and momentum conservation equations write:

$$\frac{d\rho_i}{dt} = -\rho_i \sum_{j=1}^{N} (\vec{v_j} - \vec{v_i})\vec{\nabla}_i W_{ij}\omega_j + \sum_{j=1}^{N} \vec{\psi}'_{ij}.\vec{\nabla}_i W_{ij}\omega_j, \tag{37}$$

$$\rho_i \frac{d\vec{v_i}}{dt} = \rho_i \vec{g_i} - \sum_{j=1}^{N} (P_j + P_i)\vec{\nabla}_i W_{ij}\omega_j + \sum_{j=1}^{N} \Pi'_{ij}\vec{\nabla}_i W_{ij}\omega_j. \tag{38}$$

The analogy with Eq. (27) and Eq. (29) for internal irreversible and boundary energies is proposed here as:

$$\frac{d\mathcal{E}_V}{dt} = -\mathcal{P}_{\delta'} + \sum_{i=1}^{N_{FP}} \sum_{j=1}^{N} \frac{\Pi'_{ij}}{2} (\vec{v_j} - \vec{v_i}).\vec{\nabla}_i W_{ij}\omega_i\omega_j, \tag{39}$$

$$\frac{d\mathcal{E}_{body/fluid}}{dt} = -\sum_{i=1}^{N_{FP}} \sum_{j=1}^{N_g} (P_i\vec{v_j} + P_j\vec{v_i}).\vec{\nabla}_i W_{ij}\omega_i\omega_j + \sum_{i=1}^{N_{FP}} \sum_{j=1}^{N_g} \frac{\Pi'_{ij}}{2} (\vec{v_j} + \vec{v_i}).\vec{\nabla}_i W_{ij}\omega_i\omega_j. \tag{40}$$

3.3. Summary

This section was dedicated to energy considerations inside SPH schemes. It is now possible to compute the energy transferred at the solid interface ($\mathcal{E}_{body/fluid}$). Consequently, $\mathcal{E}_{Interface}$ can also be estimated for several test cases using Eq. (4). This study aims at analysing the amount of energy introduced or dissipated compared to the other energy components. Compared to the model proposed by Cercos-Pita *et al.* [9], all energy components are directly expressed using their continuous formulations. This difference provides the addition of an extra boundary term $\mathcal{E}_V^{\partial\Omega}$ in Eq. (23):

$$\mathcal{E}_V^{\partial\Omega} = \sum_{i=1}^{N_{FP}} \sum_{j=1}^{N_g} \frac{\Pi_{ij}}{2} (\vec{v_j} - \vec{v_i})\vec{\nabla}_i W_{ij}\omega_i\omega_j. \tag{41}$$

In [9], the dissipated energy from the pressure-like term $\mathcal{P}_i = \frac{\Pi_{ij}}{2}$ does not involve the boundary conditions in the internal energy equation. However the model consistency is ensured: at convergence this term tends to disappear ($\Pi_{ij} \to 0$).

4. Energetic study of a SPH-FE coupling strategy

Two bi-dimensional test cases are considered here to analyse the energetic properties of the SPH-FE coupling strategy proposed. The influence of the dissipation parameter α_s inside the FE time integrator schemes (Newmark and HHT) is also investigated.

4.1. Deformable beam impact

The first test case proposed is a violent free surface impact of a deformable beam structure driven at high velocity [40], as illustrated in Fig. (6).

Tab. (1) summarizes the material characteristics and the simulation parameters used. The beam is made of aluminium and impacts the free surface initially at rest with an inclination angle $\beta = 10$ degrees. The motion is imposed at the two extremities with a downwards vertical velocity $V_d = 30\ m.s^{-1}$. The three markers a, b and c correspond to pressure probes. The structure mesh is composed of 4 width-wise and 40 length-wise elements. The tank is taken as sufficiently large to avoid acoustic wave reflection onto the deformable body. In order to limit the number of particles involved in this test case a varying spatial resolution is used by concentrating the finest resolution

in the impact area as proposed in [34], see Fig. (6). Note that all the equations proposed in the present paper and related to energy always imply reciprocal interactions between particles i and j, so that the scheme is intrinsically conservative. This fact still holds when using variable kernel radii (so that the energy conservation is guaranteed also in this particular case) since the discrete approximation of a function and its gradient is performed using a symmetric form by replacing R with $R_{ij} = \frac{R_i+R_j}{2}$ in $\vec{\nabla}W(\vec{x}_i - \vec{x}_j, R)$.

L	0.6 m
e	0.04 m
Young Modulus E	67.5 GPa
Poisson Coefficient ν	0.34
ρ_{beam}	2700 $kg.m^{-3}$
ρ_{water}	1000 $kg.m^{-3}$
C_0	1500 $m.s^{-1}$
CFL number	0.375
$R/\Delta x_{SPH}$	3.0

Table 1. Physical and numerical parameters for the deformable beam impact.

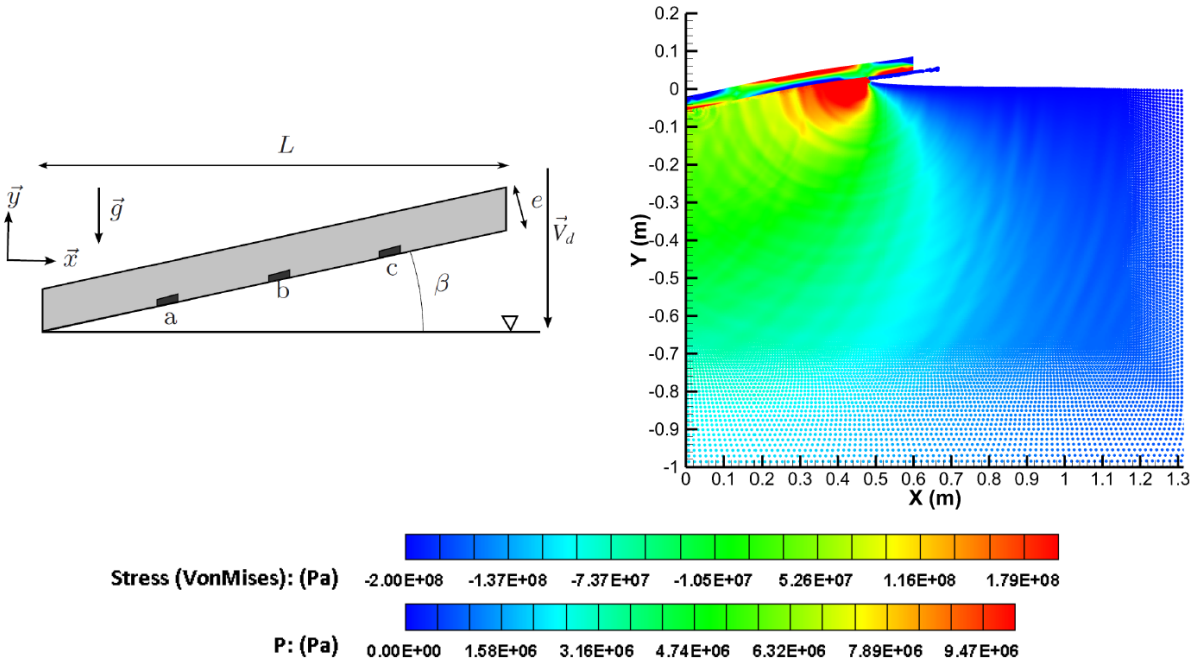

Fig. 6. Deformable beam impact configuration.

Fig. (7) provides the midpoint displacement time history of the beam for different spatial resolutions in the fluid. For Δx_{SPH} = 1 mm in the impact area, results are close to the semi-analytical solution provided in [40], obtained by combining the hydrodynamic Wagner model and a linear model of elasticity for thin shells. Good agreements are also found with results from [25] which enforced energy conservation at the fluid-structure interface. The beam deformation increases in the first instants, in accordance with the increase in pressure. It is nevertheless noted that the deformation of the plate in its midpoint finally appears slightly lower in the case of SPH-FE coupling than in the semi-analytical case. This semi-analytical model does not consider the free surface jet at the beam extremity. It can also be explained by an underestimation of the fluid pressure in the near body area according to Fig. (9). Nevertheless, note that the peak occurrence is correctly captured for Δx_{SPH} = 1 mm, as well as the pressure decrease after the peak.

Moreover, a good agreement is observed for the vertical force applied onto the deformable structure for $\Delta x_{SPH} = 1$ mm (see Fig. (8)).

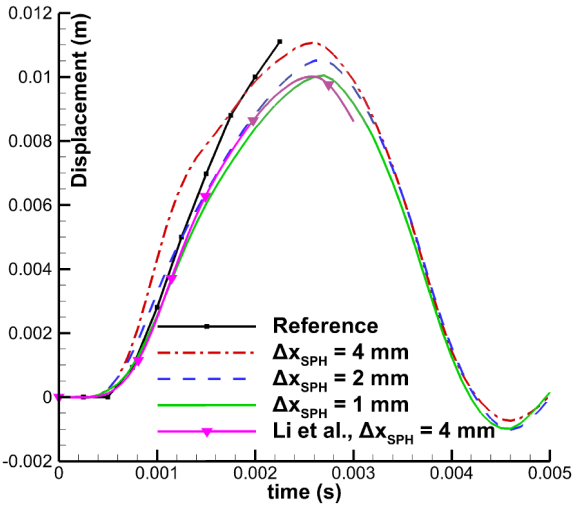

Fig. 7. Time history of the midpoint relative displacement for different spatial resolutions in the fluid, Newmark scheme with α_s = -0.3.

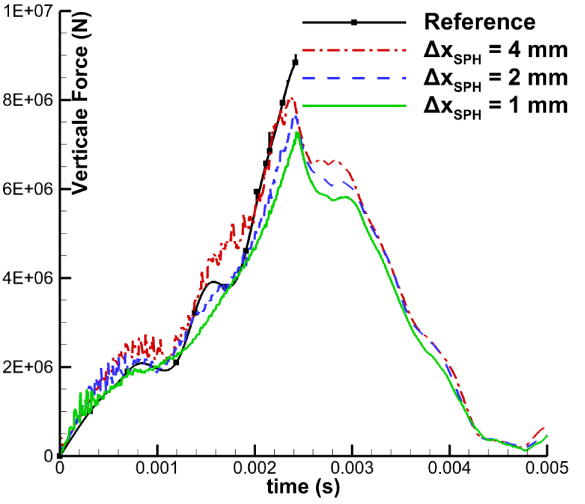

Fig. 8. Time history of vertical force on the deformable beam for different spatial resolutions in the fluid, Newmark scheme with α_s = -0.3.

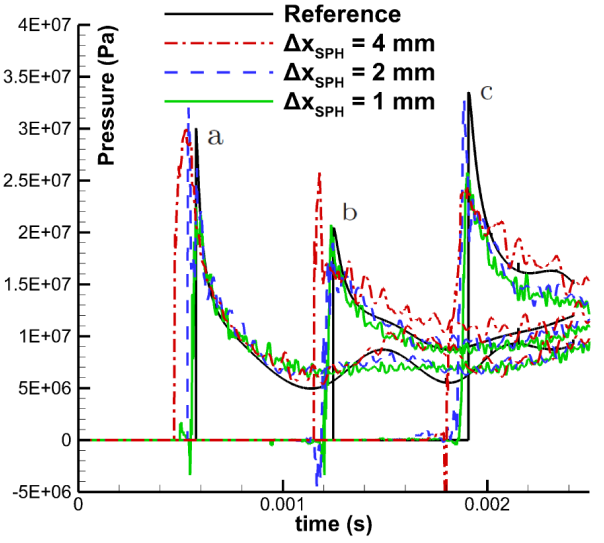

Fig. 9. Time history of the pressure probes on the deformable beam for different spatial resolutions in the fluid, Newmark scheme with α_s = -0.3.

From the energetic point of view, an energy transfer occurs from the deformable beam to the water (Fig. (10)). This energy results in fluid particle motions, visible through an increase of mechanical energy $\mathcal{E}_M$ ($\mathcal{E}_M = \mathcal{E}_P + \mathcal{E}_K$). Water particles are propelled out of the beam extremity as a high-speed free surface jet (visible in Fig. (6)). $\mathcal{E}_C$ converges quickly (see Fig. (11)). The compressible nature of the SPH scheme is used to correctly model this impact case. The fluid is first highly pressurized and then depressurized in the jet. The maximal velocity reaches 300 $m.s^{-1}$, corresponding to a Mach number of 0.2. C_0 has therefore to be chosen as equal to the actual water sound speed. This is necessary to correctly estimate the part of the energy transferred from the deformable beam which is converted into compressible energy ($\frac{d\mathcal{E}_C}{dt} > 0$) instead of mechanical energy, before being released at the end of the simulation ($\frac{d\mathcal{E}_C}{dt} < 0$). The compressible effects are not of major importance but cannot be neglected, so that an incompressible method would miss a part of the flow physics. Note that a significant amount of energy is also

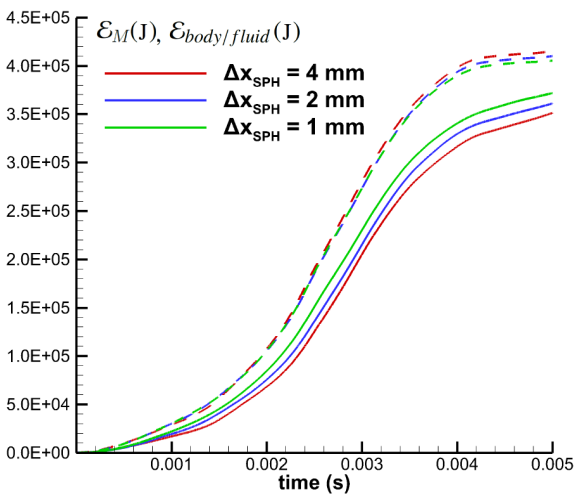

Fig. 10. Time history of $\mathcal{E}_M$ (lines) and $\mathcal{E}_{body/fluid}$ (dashed lines) of the water for different spatial resolutions in the fluid, Newmark scheme with α_s = -0.3.

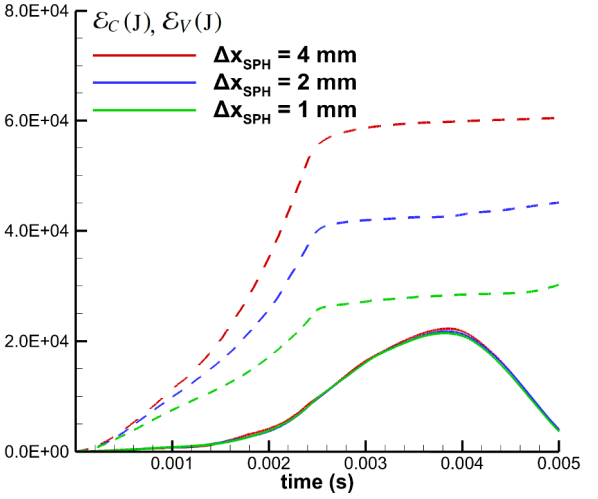

Fig. 11. Time history of $\mathcal{E}_V$ (dashed lines) and $\mathcal{E}_C$ (lines) of the water for different spatial resolutions in the fluid, Newmark scheme with α_s = -0.3.

dissipated to maintain the stability in the SPH fluid domain. According to the consistency property it decreases as the spatial resolution increases. However it tends to mask the capture of compressible effects, even with the finest spatial resolution. Nevertheless, in this configuration $\mathcal{E}_C + \mathcal{E}_V$ is about 10% of $\mathcal{E}_M$. The energy errors from EV remain therefore acceptable using Δx_{SPH} = 1 mm.

Concerning the coupling interface energy, Fig. (12) shows that the fluid receives less energy with the ghost particle method ($\mathcal{E}_{body/fluid}$) than the energy lost by the aluminium beam through pressure forces ($\mathcal{E}_{fluid/body}$). Following Eq. (4), $\mathcal{E}_{Interface}$ is negative. Note that $\frac{d\mathcal{E}_{body/fluid}}{dt}$ is strictly equal to $\frac{d\mathcal{E}_{TOT}}{dt}$ according to Eq. (28). Fig. (13) shows the energy variation in the global domain $\Delta\mathcal{E}_{F+S} = (\mathcal{E}_{TOT} + \mathcal{E}_S) - (\mathcal{E}^0_{TOT} + \mathcal{E}^0_S)$ compared to the energy yielded from the outside $\mathcal{E}_{Outside}$, where $\mathcal{E}_S$ is the solid total energy deduced from *Code_Aster* outputs. $\mathcal{E}_{Outside}$ corresponds to the energy brought to impose a constant velocity (30 $m.s^{-1}$) on the beam, which is estimated using the FE solver outputs. The global system loses energy through the fluid-structure interface. This phenomenon can lead to severe problems. Indeed, the accumulation of energy errors can modify the accuracy and the stability of the solution. Note that Fig. (12) and Fig. (13) are very similar. This was expected since $\mathcal{E}_{Outside}$ mostly depends on the energy recovered by the water from the FE point of view (i.e. $\mathcal{E}_{fluid/body}$) in order to maintain a constant velocity (30 $m.s^{-1}$) on the beam. Furthermore, $\Delta\mathcal{E}_{F+S}$ represents the energy variation in the global domain, which mainly corresponds to the fluid energy variation (i.e. $\mathcal{E}_{body/fluid}$). Only a small part is taken over by the beam principally through elastic energy. Note that $\mathcal{E}_{fluid/body}$ displays a lower convergence rate than $\mathcal{E}_{body/fluid}$, so that $\mathcal{E}_{fluid/body}$ requires a higher spatial resolution to converge. However the adopted spatial resolution is sufficiently high to correctly simulate this deformable beam impact (Fig. (8)). Furthermore, the consistency of our model seems ensured as both $\mathcal{E}_{fluid/body}$ and $\mathcal{E}_{body/fluid}$ tend to converge towards the same value.

Strong variations of $\mathcal{E}_{Interface}$ occur during the impact, as visible in Fig. (14). From t = 0 ms to t = 1.5 ms, $\mathcal{E}_{Interface}$ represents more than 20% of $\mathcal{E}_{TOT}$. At the beginning of the impact errors are close to be equal to $\mathcal{E}_{TOT}$ for Δx_{SPH} = 1 mm. For coarser fluid spatial resolutions, the maximum ratio is lower because $\mathcal{E}_{TOT}$ is higher. However, Fig. (12) shows that the total energy is very small at this stage (order of 10^4 J) compared to the following (order of 10^5 J). The simulation remains therefore acceptable despite of these important errors, at least for the highest spatial resolution. Δx_{SPH} = 1 mm is clearly just sufficient, coarser resolutions are not acceptable. For the finest resolution, the energy ratio quickly decreases under 0.1 after t = 1.5 ms. It finally converges towards a value close to 7% of $\mathcal{E}_{TOT}$. At this time $\mathcal{E}_{Interface}$ has the same energy level as $\mathcal{E}_V$ (see Fig. (15)). Fig. (15) shows that varying the parameter α_s in the FE time integrator scheme has no influence on the solution for α_s < -0.05 with the Newmark scheme. However in practice $\alpha_s \leq$ -0.1 is needed for stability purposes using the HHT scheme. Instabilities appear for lower values of α_s, [17], leading to divergences of $\mathcal{E}_{Interface}$.

Fig. (16) compares the vertical force time histories for HHT and Newmark schemes for different values of the

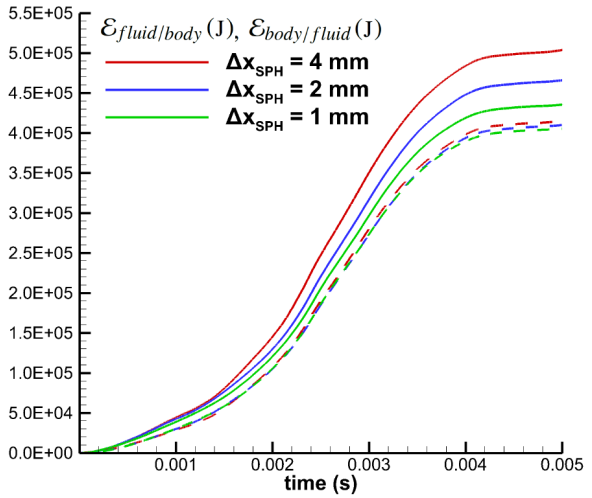

Fig. 12. Time history of $\mathcal{E}_{fluid/body}$ (lines) and $\mathcal{E}_{body/fluid}$ (dashed lines) for different spatial resolutions in the fluid, Newmark scheme with α_s = -0.3.

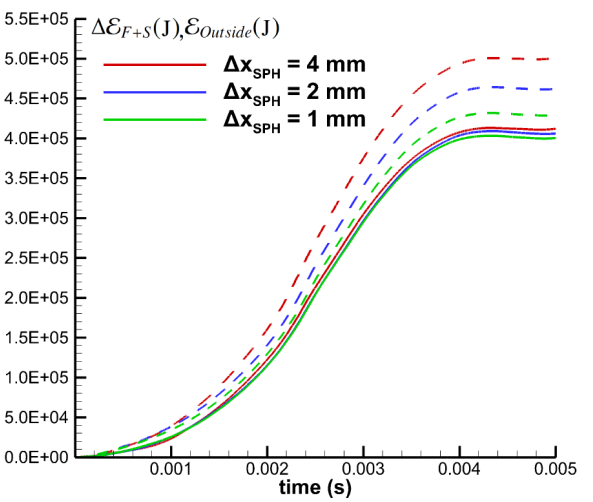

Fig. 13. Time history of $\Delta\mathcal{E}_{F+S}$ (lines) and $\mathcal{E}_{Outside}$ (dashed lines) for different spatial resolutions in the fluid, Newmark scheme with α_s = -0.3.

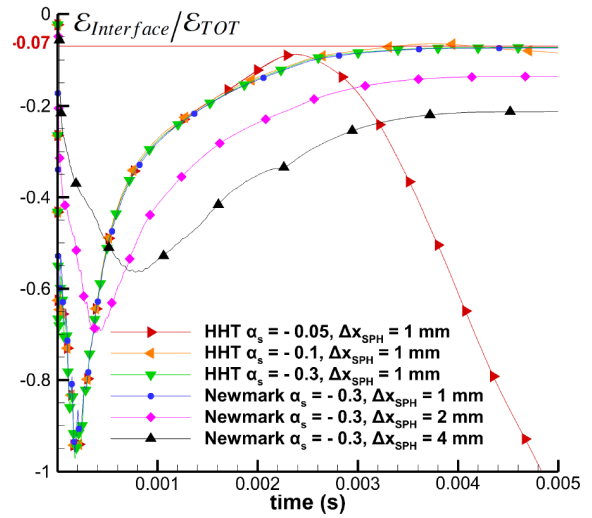

Fig. 14. Time history of ratio between $\mathcal{E}_{Interface}$ and $\mathcal{E}_{TOT}$ for different stabilization coefficients.

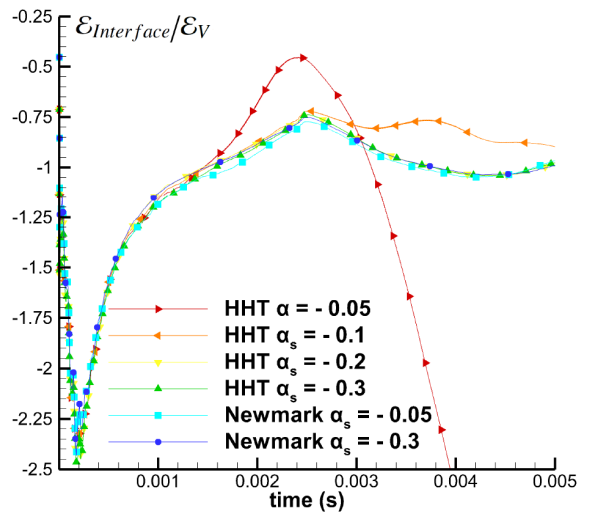

Fig. 15. Time history of ratio between $\mathcal{E}_{Interface}$ and $\mathcal{E}_{V}$ for different stabilization coefficients, Δx_{SPH} = 1 mm.

dissipation parameter α_s. High frequency oscillations are observed for low dissipation values in the HHT scheme, although the energy evolution matches with the coupling stability criterion described in [17].

Fig. (17) confirms the above statements, by presenting snapshots of the computed solution at various instants with different FE time integrator schemes. These snapshots are plotted with pressure and Von Mises stress contours respectively for the fluid and the structure. Strong non physical perturbations are observed in the pressure field for HHT with $\alpha_s = -0.05$ (especially after $t = 2$ ms), leading to strong vertical oscillations as visible in Fig. (16). In this configuration, increasing the stabilization parameter α_s helps in maintaining a stable coupling.

4.2. Dam-break flow trough an elastic gate

A case involving relatively low dynamics is considered here. The fluid initially at rest is contained within a rigid tank closed using an elastic gate on the left side. At $t = 0$ s the elastic gate is released to let the water escape. This test case has been first introduced by Antoci [1], according to the configuration presented in Fig. (18) and Tab. (2). In

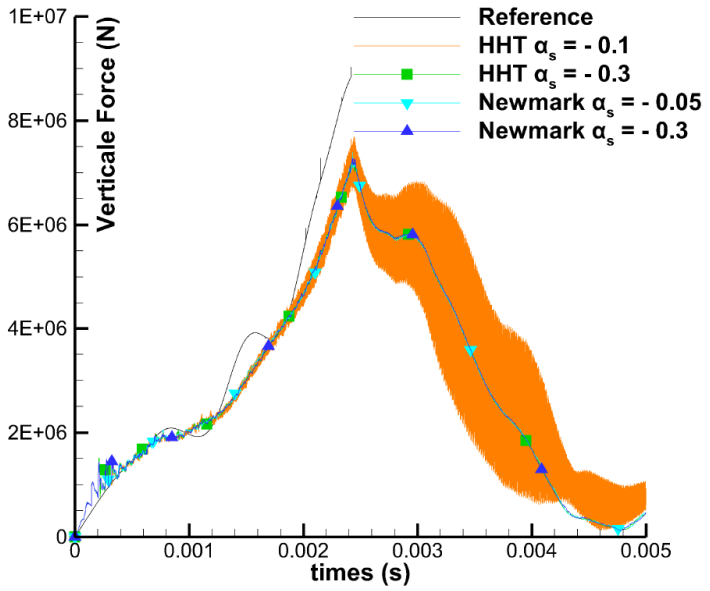

Fig. 16. Time history of the vertical force on the beam for different stabilization coefficients, Δx_{SPH} = 1 mm.

their study, Antoci [2] used a monolithic approach with a SPH-SPH coupling to model this FSI problem and proposed some comparisons with their experimental data.

In the present work, fluid particles are distributed uniformly, and finite elements are used to model the elastic gate. The FE mesh is composed of 4 width-wise and 40 length-wise elements. The behaviour of rubber is considered as incompressible with a Poisson coefficient close to 0.5, and the non-linear strain-stress curve obtained experimentally is used to characterize its behaviour (Fig. (19)).

L	79 mm
H	0.14 m
e	5 mm
l	0.1 m
Poisson Coefficient	≈ 0.5
ρ_{rubber}	1100 $kg.m^{-3}$
ρ_{water}	1000 $kg.m^{-3}$
g	9.81 $m.s^{-2}$

ΔX_{FE}	1.25 mm
ΔY_{FE}	1.975 mm
$R/\Delta x_{SPH}$	4.0
C_0	30 $m.s^{-1}$
CFL number	0.375

Table 2. Physical and numerical parameters of the Antoci dam break.

Fig. (20) compares the experimental and numerical time histories of the gate tip displacements for a stabilization coefficient $\alpha_s = -0.3$ in the Newmark scheme. Numerical results are in good agreement with the experiments from [2], even with the coarsest resolution (Δx_{SPH} = 1 mm). In particular, the global trend of the gate deformation time history is correctly captured. A small offset can be noticed but it tends to decrease as the spatial resolution increases. The abrupt decrease of the displacement observed experimentally from instant t = 0.32 s is not reproduced using our coupling, but it can be attributed to a leakage of fluid between the tank and the gate visible on the experimental snapshots. Numerical results are also in good agreement with [25], where the energy conservation is enforced at the interface. The differences observed can be explained by small discordances in the rubber material law.

From the energetic point of view, the water transfers its energy to the gate which is converted into elastic energy (Fig. (21)). The flow is purely incompressible ($\mathcal{E}_C$ is negligible). In the simulation, the initial water potential energy is thus mainly converted into kinetic energy (Fig. (22)), but a small part is lost through the boundary conditions (Fig. (23)). Note that $\mathcal{E}_S$, $\mathcal{E}_P$ and $\mathcal{E}_K$ are already converged with the coarsest fluid spatial resolution. The energy lost through fluid boundary conditions (exactly equal to the variations of $\mathcal{E}_{TOT}$) is lower than the energy provided to the

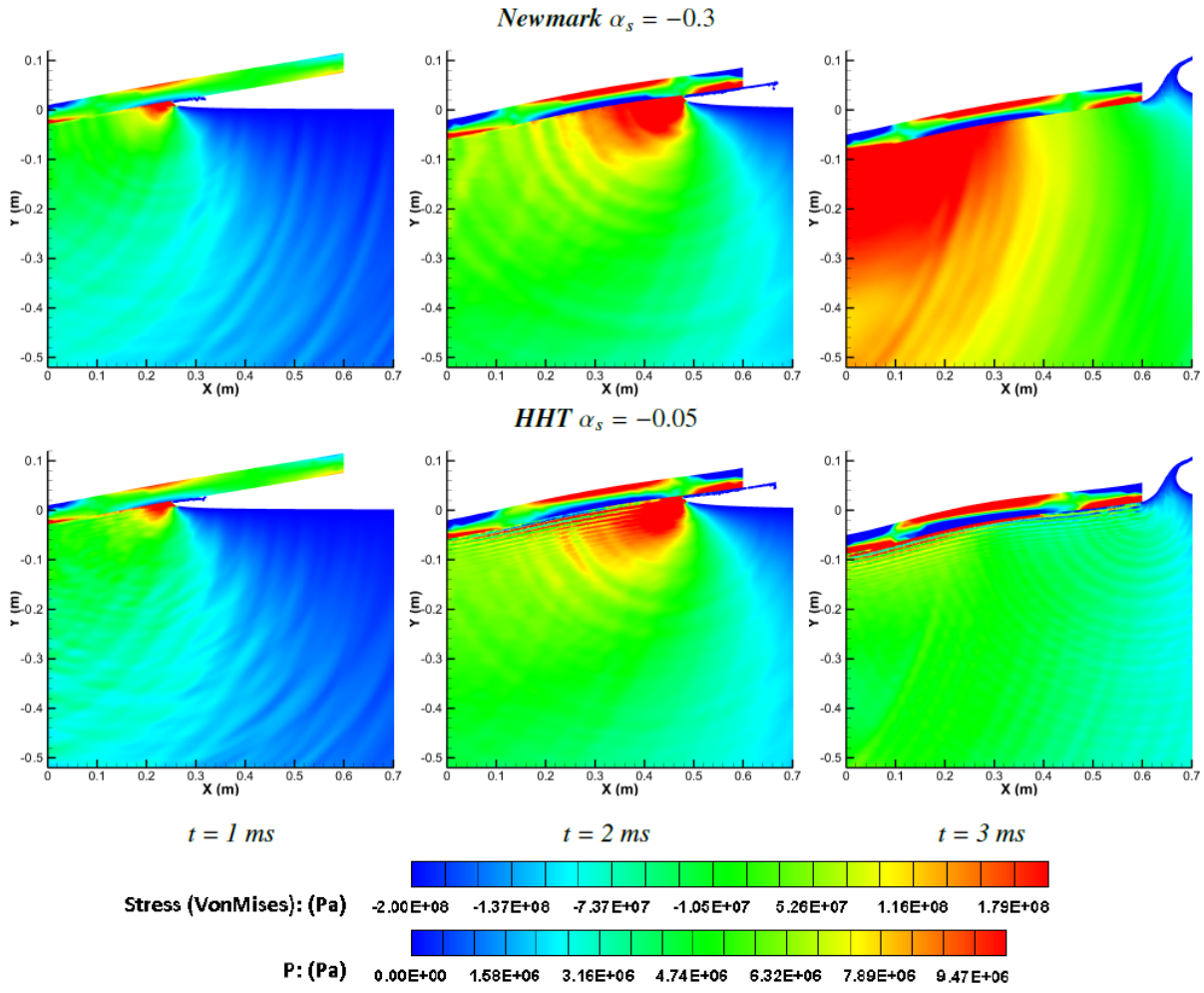

Fig. 17. Pressure field comparisons between different stabilization coefficients (rows) for different instants (columns), Δx_{SPH} = 1 mm.

elastic gate by pressure forces (see Fig. (23)). Consequently, an unexpected additional energy is introduced at the body interface. $\mathcal{E}_{Interface}$ is therefore positive and the total energy is slightly increased. Fig. (24) shows the energy variation of the global domain $\frac{\mathcal{E}_{F+S}-\mathcal{E}^0_{F+S}}{\mathcal{E}^0_{F+S}}$ which increases while no energy is introduced from the outside. However the consistency of our model seems ensured since $\frac{\mathcal{E}_{F+S}-\mathcal{E}^0_{F+S}}{\mathcal{E}^0_{F+S}}$ tends towards zero as the spatial resolution increases.

Fig. (25) shows the ratio between $\mathcal{E}_{Interface}$ and $\mathcal{E}_{TOT}$ with different solid time integration schemes (Newmark and HHT). As proved in [17], a small dissipation modifies the coupling stability, so that some instabilities tend to appear at low dissipation levels in the solid. For HHT coefficient α_s = -0.1, $\mathcal{E}_{Interface}$ increases much faster than for higher stabilization levels. Fig. (26) shows the displacement of the gate tip for various values of the stabilization parameter and confirms that the displacement is strongly erroneous with the HHT scheme using α_s = -0.1. Instabilities in the structure solution lead to high frequency displacements of the interface, and are responsible for non physical acoustic waves within the fluid (Fig. (27)).

All other cases plotted in Fig. (25) show negligible energy errors (less than 1%) when compared to $\mathcal{E}_{TOT}$. Nevertheless, as shown in Fig. (28) $\mathcal{E}_{Interface}$ still displays strong errors with respect to EV even using the finest spatial resolution. At the beginning of the simulation, errors are close to be equal to 18 times $\mathcal{E}_V$ (see Fig. (29)). However, $\mathcal{E}_V$ is very small at this stage (order of 10^{-3} J) compared to the following (order of 10^{-2} J). Then this ratio quickly decreases under the value 2 for $t > 0.15$ s. These simulations therefore remain acceptable although large apparent errors appear at the first instants. Furthermore, $\mathcal{E}_{Interface}$ tends to diverge for low numerical diffusion levels while

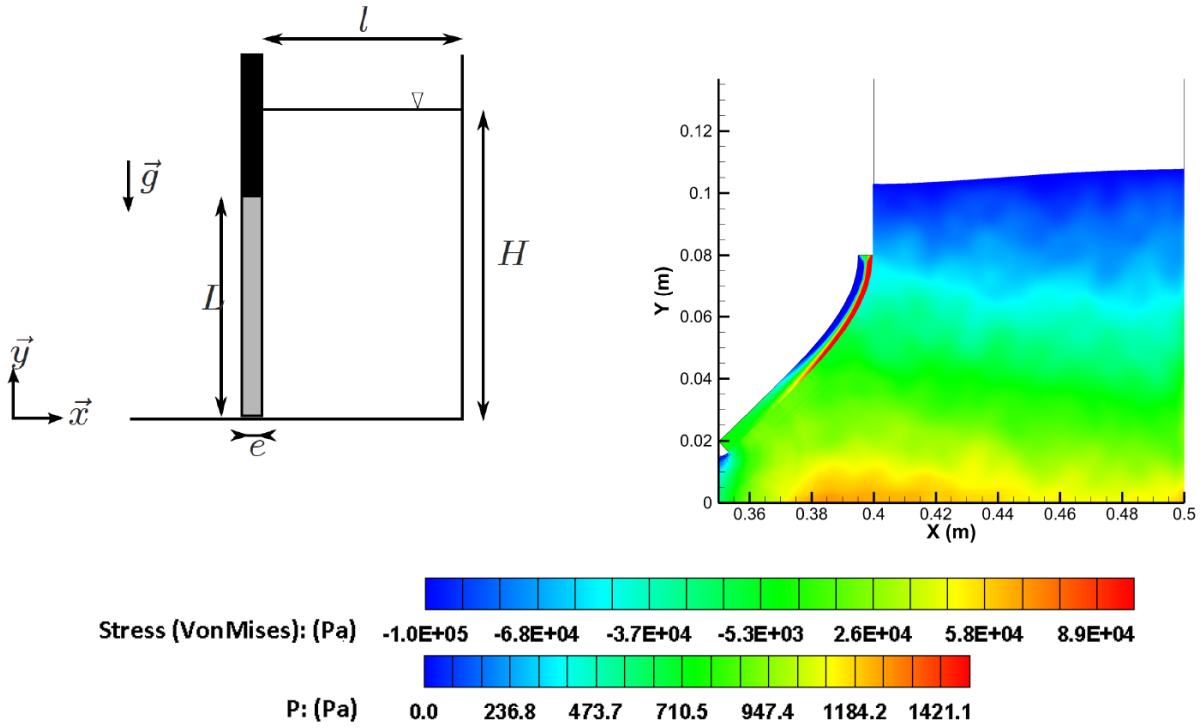

Fig. 18. Antoci [1] dam-break configuration.

using the HHT scheme.

5. Coupling improvements

5.1. Fluid-structure loading

The previous section emphasized the non conservation of interface energy and outlined the need for improving the coupling scheme proposed. A correction criterion or a new loading method is needed to overcome these limitations and to improve the coupling robustness and accuracy. For algorithmic simplicity and genericity purposes, we chose to avoid any hard-coding within the FE solver. The improvements proposed address exclusively fluid pressure loads provided to the FE solver and interface energy conservation.

5.1.1. Force conservative formulation

Our first approach consisted in determining fluid pressure loads as an average of neighborhood pressure performed through Eq. (1). The second approach proposed here resides in ensuring reciprocal forces between fluid and solid media. This is achieved through the summation of ghost particle interactions with fluid particles, as proposed for instance in [14] and [7, 27] for rigid bodies. The force can be expressed as:

$$\vec{F}_{fluid/body} = -\vec{F}_{body/fluid} = -\sum_{i=1}^{N_{FP}} \sum_{j=1}^{N_g} [-P_i - P_j + \Pi'_{ij}] \vec{\nabla}_i \omega_i \omega_j, \tag{42}$$

Obviously in the case of a deformable body this force should be decomposed on each panel k, so that:

$$\vec{F}_{fluid/body} = \sum_{k=1}^{N_p} \vec{F}^k_{fluid/body}, \tag{43}$$

with

$$\vec{F}^k_{fluid/body} = -\sum_{i=1}^{N_k} \sum_{j=1}^{N_P} [-P_i - P_j + \Pi'_{ij}] \vec{\nabla}_i \omega_i \omega_j, \tag{44}$$

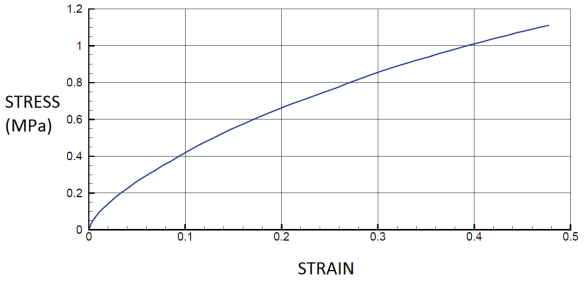

Fig. 19. Strain-stress curve for the rubber used.

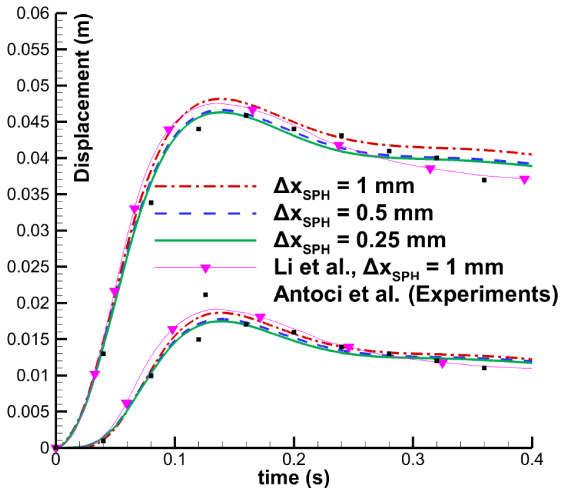

Fig. 20. Time history of the horizontal (top) and vertical (bottom) displacements of the gate tip for different fluid resolutions compared to experiments, Newmark scheme with α_s = -0.3.

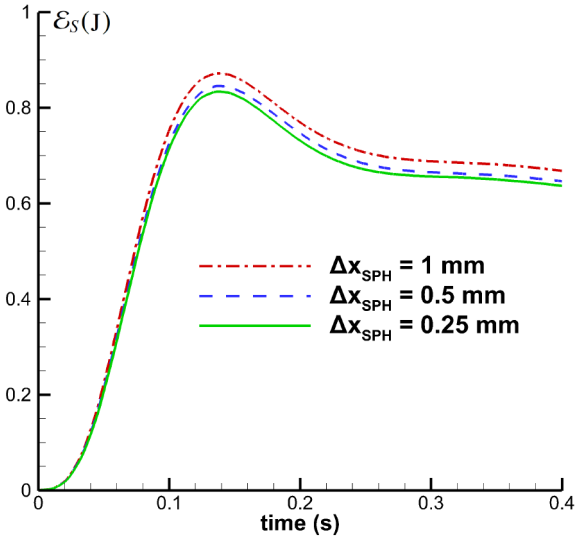

Fig. 21. Time history of solid total energy for different fluid spatial resolutions, Newmark scheme with α_s = -0.3.

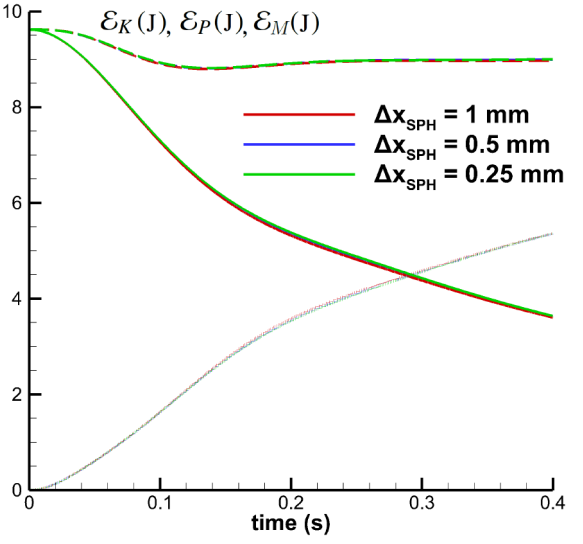

Fig. 22. Time history of $\mathcal{E}_M$ (dashed lines), $\mathcal{E}_K$ (dotted lines) and $\mathcal{E}_P$ (lines) for different fluid spatial resolutions, Newmark scheme with α_s = -0.3.

where N_P is the number of panels and N_k is the set of particles seen by the panel k (see Fig. (2)). As the calculation of ghost interactions is needed anyway for imposing boundary conditions, pressure forces $\vec{F}^k_{fluid/body}$ are transferred to the FE solver at the end of each first Runge-Kutta stage. Note that this improvement does not directly come from the energy analysis. Nevertheless, it is closely linked to this analysis through the contributions of boundary forces in the energy balance.

5.1.2. Energy conservative formulation

An energy conservative exchange at the interface is also considered. At each instant, it is possible to compute the boundary energy $\mathcal{E}_{body/fluid}$ of the previous time step. A corrective coefficient ϵ can be introduced in the force

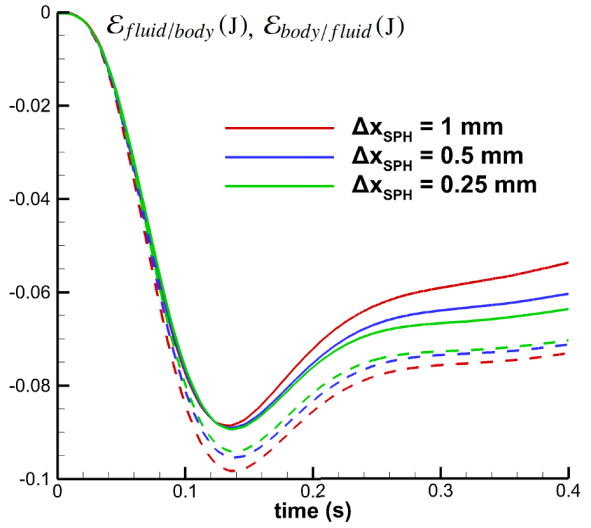

Fig. 23. Time history of ratio between $\mathcal{E}_{fluid/body}$ (dashed lines), $\mathcal{E}_{body/fluid}$ (lines) for different fluid spatial resolutions, Newmark coefficient α_s = -0.3.

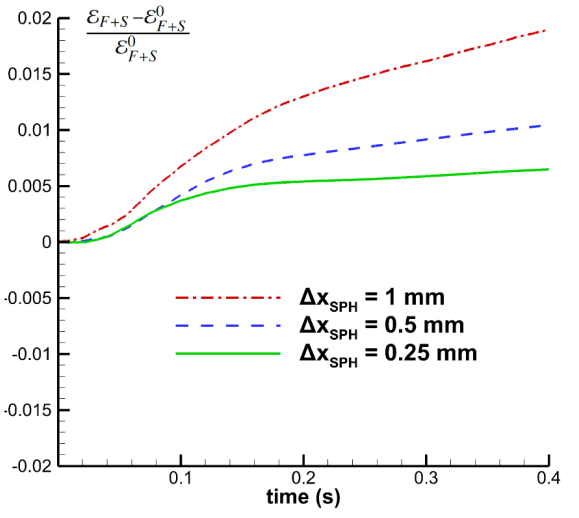

Fig. 24. Time history of $\frac{\mathcal{E}_{F+S}-\mathcal{E}^0_{F+S}}{\mathcal{E}^0_{F+S}}$ for different fluid spatial resolutions, Newmark scheme with α_s = -0.3.

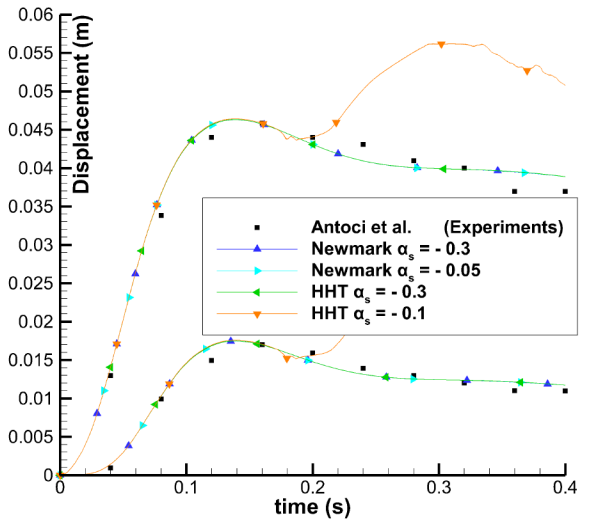

Fig. 25. Time history of ratio between $\mathcal{E}_{Interface}$ and $\mathcal{E}_{TOT}$ for different stabilization coefficients, Δx_{SPH} = 0.25 mm.

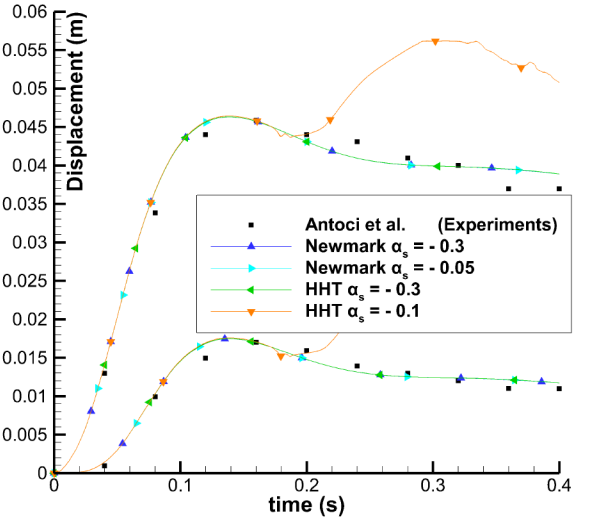

Fig. 26. Time history of the horizontal (top curve) and vertical (bottom curve) displacements of the gate tip for different stabilization coefficients, Δx_{SPH} = 0.25 mm.

$\vec{F}^{\epsilon}_{fluid/body}$ calculation as:

$$\vec{F}^{\epsilon}_{fluid/body} = -(1+\epsilon)\sum_{i=1}^{N_k}\sum_{j=1}^{N_g}[-P_i - P_j + \Pi'_{ij}]\vec{\nabla}_i\omega_i\omega_j. \tag{45}$$

The new variations of the boundary energy transmitted from the fluid to the body $\mathcal{E}^{\epsilon}_{fluid/body}$ can be expressed as:

$$\frac{d\mathcal{E}^{\epsilon}_{fluid/body}}{dt} = \sum_{k=1}^{N_p}\left[-(1+\epsilon)\sum_{i=1}^{N_k}\sum_{j=1}^{N_g}[-P_i - P_j + \Pi'_{ij}]\vec{\nabla}_i\omega_i\omega_j.\vec{v}_k\right] = (1+\epsilon)\frac{d\mathcal{E}_{fluid/body}}{dt}. \tag{46}$$

On the contrary the variation of $\mathcal{E}_{body/fluid}$ remains unchanged since it does not depend on ϵ. The coefficient ϵ is

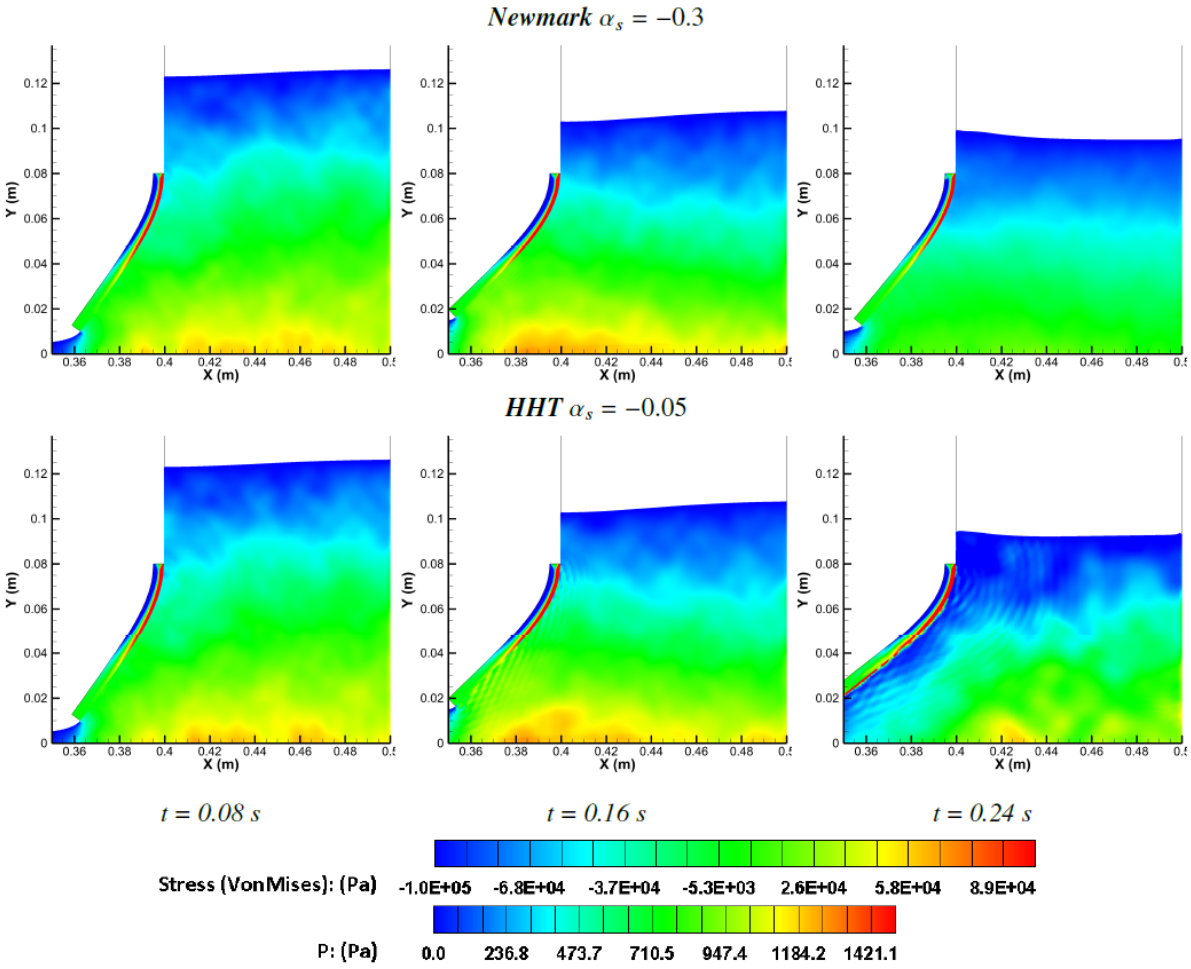

Fig. 27. Pressure field comparisons between different stabilization coefficients (rows) at different instants (columns), Δx_{SPH} = 0.25 mm.

chosen to impose the same evolution for $\mathcal{E}_{fluid/body}$ and $\mathcal{E}_{body/fluid}$ leading to:

$$\mathcal{E}_{fluid/body} + \frac{d\mathcal{E}^{\epsilon}_{fluid/body}}{dt}\Delta t = \mathcal{E}_{body/fluid} + \frac{d\mathcal{E}_{body/fluid}}{dt}\Delta t, \tag{47}$$

which means that

$$\epsilon = \frac{\mathcal{E}_{body/fluid} - \mathcal{E}_{fluid/body} + (\frac{d\mathcal{E}_{body/fluid}}{dt} - \frac{d\mathcal{E}_{fluid/body}}{dt})\Delta t}{\frac{d\mathcal{E}_{fluid/body}}{dt}\Delta t}. \tag{48}$$

Usually, the rate of change of $\mathcal{E}_{fluid/body}$ and $\mathcal{E}_{body/fluid}$ are similar so that ϵ remains small and does not need to be limited. Nevertheless, in some cases the rate of change of $\mathcal{E}_{fluid/body}$ can strongly differ from $\mathcal{E}_{body/fluid}$, leading to possibly large values of ϵ and resulting in a sudden change in the time evolution of $F_{fluid/body}$. Numerical tests showed that the value of ϵ should be limited as proposed in Eq. (49) to avoid such an effect and to preserve the stability of the coupling.

$$-0.15 < \epsilon < 0.15. \tag{49}$$

5.2. Numerical validations

5.2.1. Deformable beam impact

The deformable beam impact is performed here with the above improvements and using the same spatial fluid resolution Δx_{SPH} = 1 mm. In the last section coupling errors tended to be higher than 7% of $\mathcal{E}_{TOT}$ using the averaging

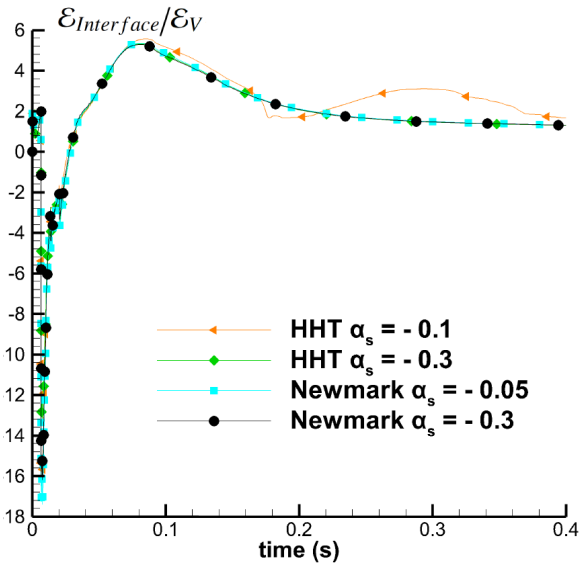

Fig. 28. Time history of ratio between $\mathcal{E}_{Interface}$ and $\mathcal{E}_V$ for different stabilization coefficients, Δx_{SPH} = 0.25 mm.

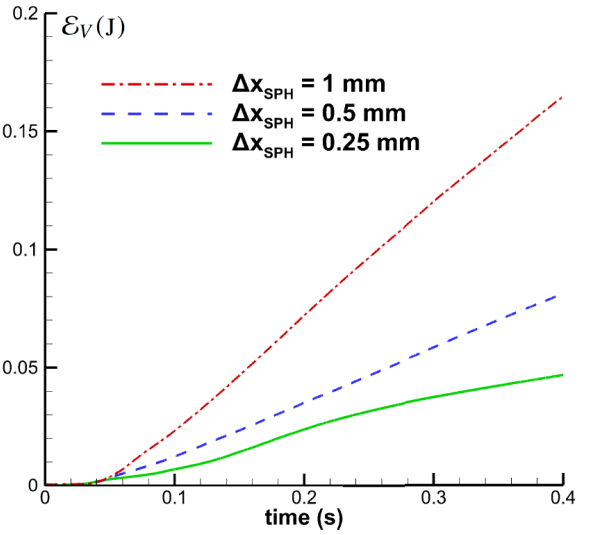

Fig. 29. Time history of $\mathcal{E}_V$ for different fluid spatial resolutions

pressure technique (see Fig. (14)). Using the force conservative formulation, $\mathcal{E}_{Interface}$ is still negative (the global system still lose some energy through the fluid structure interface), but energy errors converge towards a value close to 2.8% of $\mathcal{E}_{TOT}$ (see Fig. (30)). The accumulation of energy errors is therefore reduced thanks to the force conservation formulation. Another advantage of this approach is to avoid any overestimation of forces in cases where only few particles are located in the near panel area. Only ghost particle forces on the panel k are considered, and pressure loads are therefore more accurate. As a consequence the ratio between $\mathcal{E}_{Interface}$ and $\mathcal{E}_V$ is also strongly decreased (Fig. (30)), as it is now close to 0.4 instead of 1.4 in Fig. (15).

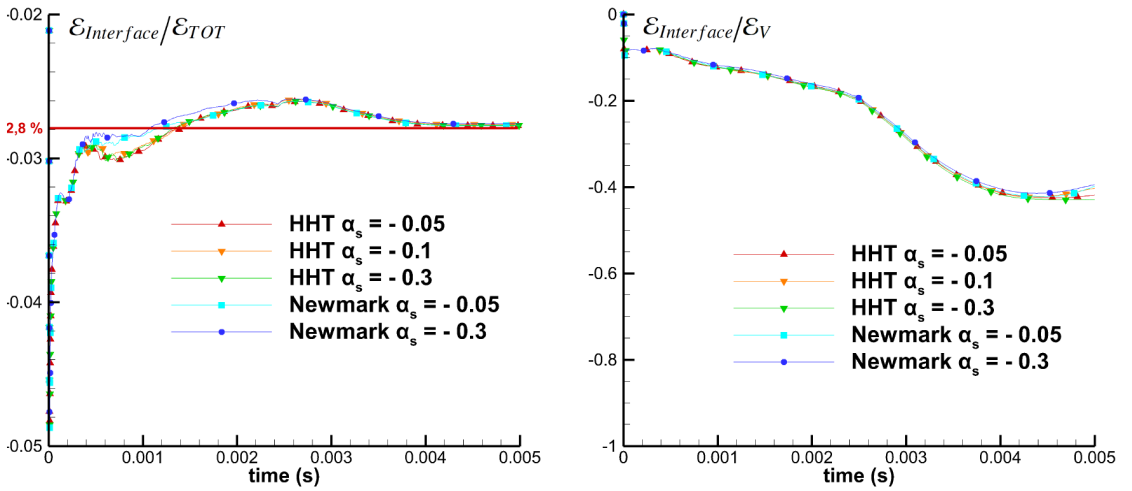

Fig. 30. Time history of ratios between $\mathcal{E}_{Interface}$ and $\mathcal{E}_{TOT}$ (left) and between $\mathcal{E}_{Interface}$ and $\mathcal{E}_V$ (right) for different stabilization coefficients, force conservative formulation.

Fig. (31) presents the time history of the same energy ratios, but obtained this time with the energy conservative formulation. Energy ratios converge towards zero at the end of the simulation and $\mathcal{E}_{Interface}$ is not strictly equal to zero due to the limitation imposed on the corrective coefficient ϵ. Nevertheless it quickly converges towards zero in all cases, emphasizing the benefits of such improvements. Note also that the $\mathcal{E}_{Interface} > 0$ here, the corrective coefficient ϵseems underestimated. Nevertheless the origin of this effect should be further investigated.

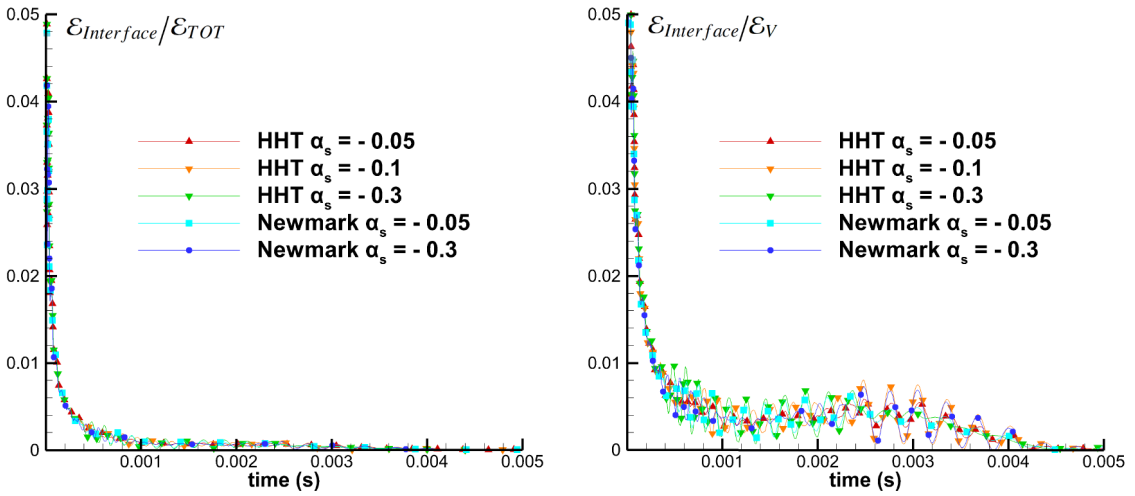

Fig. 31. Time history of ratios between $\mathcal{E}_{Interface}$ and $\mathcal{E}_{TOT}$ (left) and between $\mathcal{E}_{Interface}$ and $\mathcal{E}_{V}$ (right) for different stabilization coefficients, energy conservative formulation.

The robustness property of the SPH-FE coupling strategy is therefore strongly improved. Indeed the SPH-FE coupling is more stable for lower dissipative coefficients α_s in the HHT scheme: even HHT with $\alpha_s = -0.05$ provides correct results, contrary to the first implementation. $\mathcal{E}_{Interface}$ is no more affected by the dissipation in the structure part. Varying the parameter α_s does not have a significant influence on the solution behaviour. Instabilities which appeared at low dissipation levels in the solid with the averaging pressure technique (Fig. (14) and Fig. (15)) are absent here. The coupling is stable for any α_s parameter values and whatever the time scheme used (HHT or Newmark). High frequency oscillations vanished from the fluid force time history for low dissipation values in the HHT scheme (see Fig. (32), where the results using the averaging pressure is recalled).

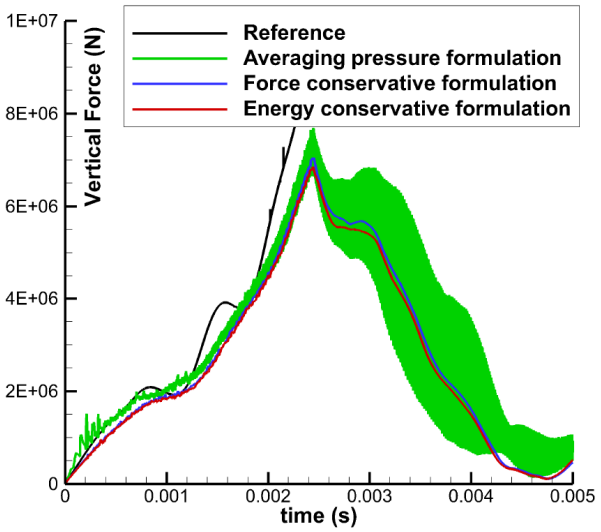

Fig. 32. Time history of vertical force on the deformable beam for different load formulations, HHT scheme with $\alpha_s = -0.1$.

Fig. (33) presents some snapshots of the computed solutions for the various formulations discussed in this paper. These snapshots are plotted with pressure and Von Mises stress contours respectively for the fluid and the solid. Using the averaging pressure procedure, the numerical diffusion introduced by the HHT is not sufficient. As a result the high frequency displacement of the deformable body interface generates some acoustic waves in the fluid. Using the force and energy conservation procedures proposed here, pressure loads are more accurate and regular. Less diffusion is

therefore needed to obtain a robust coupling. The pressure field is slightly more regular with the energy conservation procedure, especially at $t = 2$ ms as shown in Fig. (33).

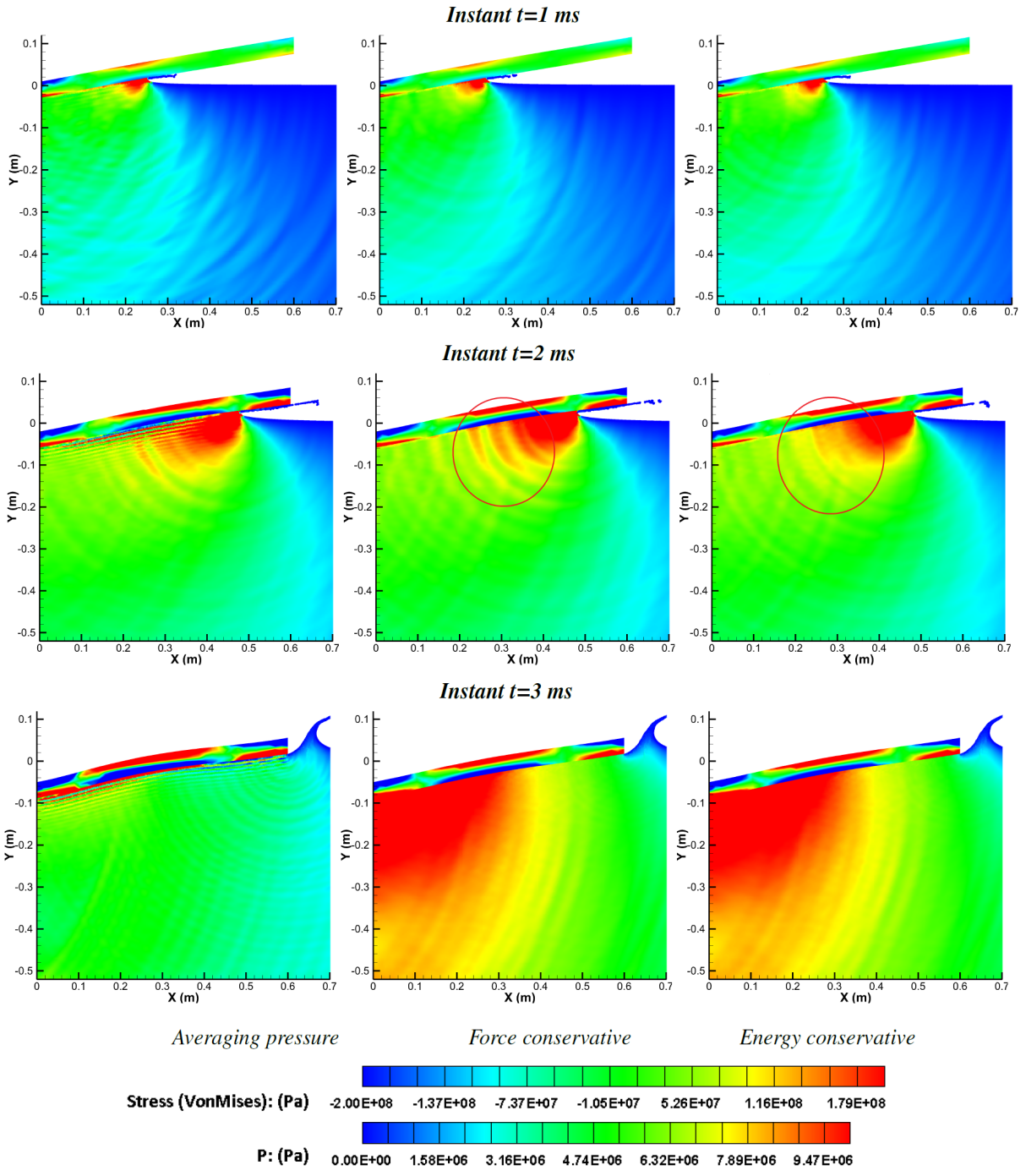

Fig. 33. Pressure field comparison for different load formulations (columns) at different instants (lines), HHT scheme with $\alpha_s = -0.05$.

5.2.2. Dam-break flow through an elastic gate

The dam-break flow through an elastic gate is performed using a spatial resolution $\Delta x_{SPH} = 0.25$ mm in the fluid. Here again, the accumulation of energy errors has been strongly reduced using the conservation improvements

proposed (Fig. (34) and Fig. (35)). It is particularly visible on the ratio between $\mathcal{E}_{Interface}$ and $\mathcal{E}_V$.

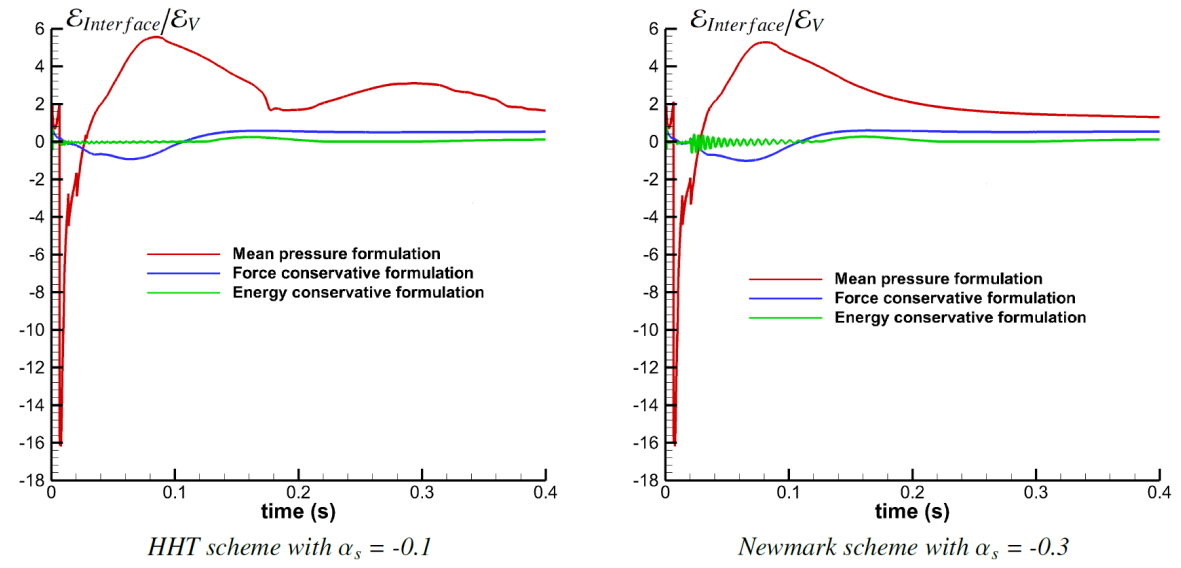

Fig. 34. Time history of ratios between $\mathcal{E}_{Interface}$ and $\mathcal{E}_V$ for different stabilization coefficients.

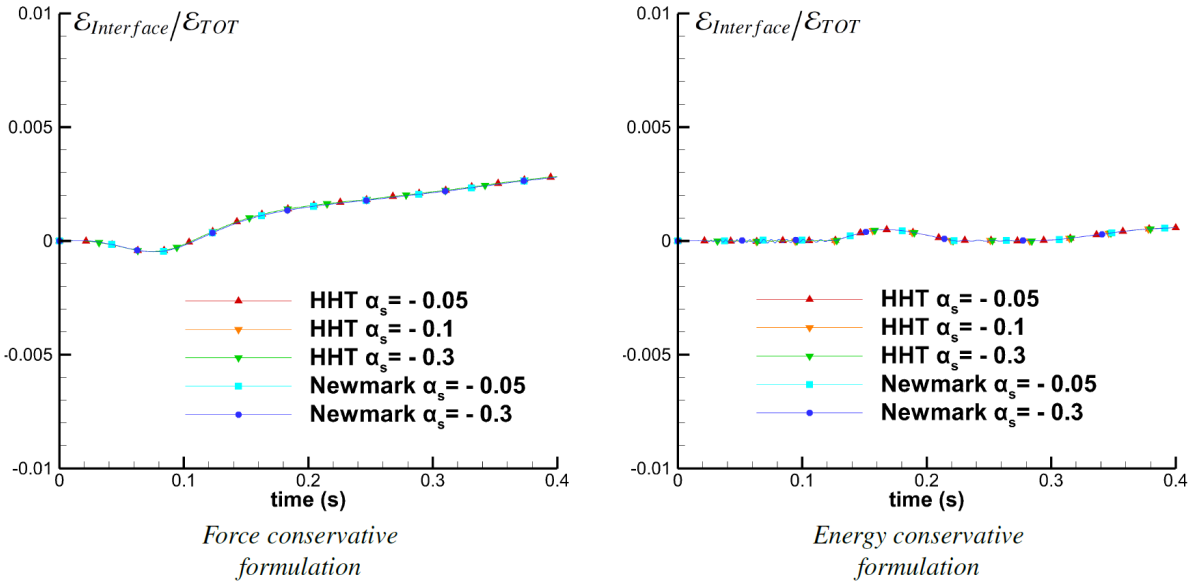

Fig. 35. Time history of ratios between $\mathcal{E}_{Interface}$ and $\mathcal{E}_{TOT}$ for different stabilization coefficients.

Both formulations increase the coupling robustness regarding the lowest dissipation levels in the FE time integrator scheme. Numerical stability is maintained even at low stabilization coefficients (Fig. (36)). Force and energy conservative formulations show good agreements with the experimental data, but also with the numerical results from [25] which enforce energy conservation at the fluid-structure interface using a very different approach. This test cases hows two main phases: from $t = 0$ s to $t \approx 0.14$ s the fluid yields its energy to the elastic gate, Fig. (37) (i.e the elastic gate is pushed). Then the solid gate gives back a part of its energy to the fluid from $t \approx 0{:}14$ s to $t = 0.4$ s. Regarding the force time history, both formulations provide slightly different results (see Fig. (38)). During the first phase, the dynamics of the flow are the same. $\mathcal{E}_{Interface}$ is very small and both formulations provide similar results. In the second

phase, some differences appear as the gate comes back. Using the energy conservative formulation, the elastic gate tends to come back more slowly (Fig. (37)), as the force is increased to be in energy agreement.

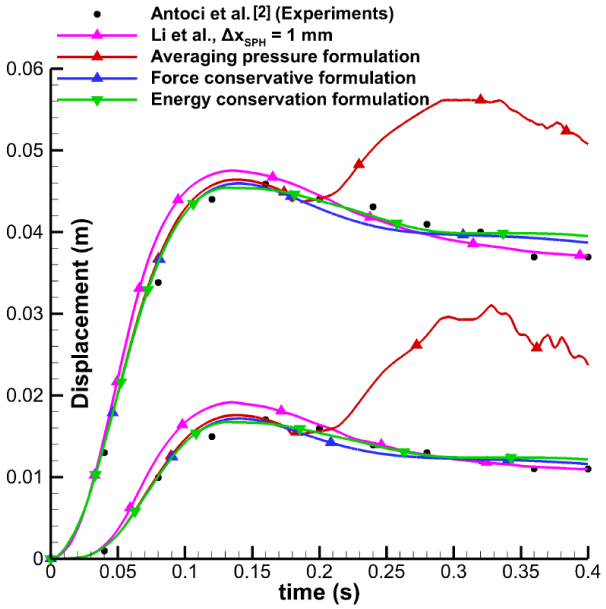

Fig. 36. Time history of horizontal (top) and vertical (bottom) displacements of the gate tip for the different formulations proposed, HHT scheme with $\alpha_s = -0.1$.

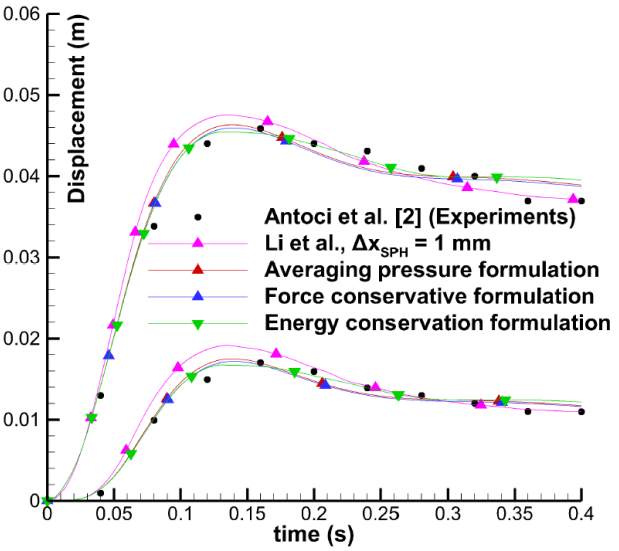

Fig. 37. Time history of horizontal (top) and vertical (bottom) displacements of the gate tip for the different formulations proposed, Newmark scheme with $\alpha_s = -0.3$.

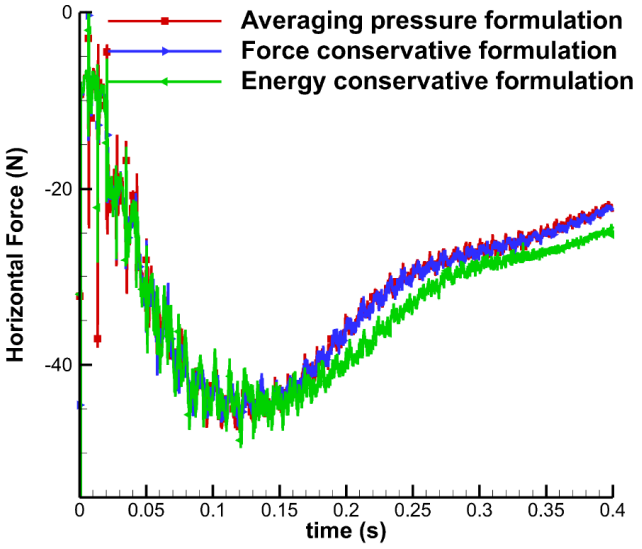

Fig. 38. Time history of horizontal force on the elastic gate for the different formulations proposed, Newmark scheme with $\alpha_s = -0.3$.

Fig. (39) shows some snapshots of the computed solution for the different formulations proposed. It highlights the benefits of the new loading formulations compare to the averaging pressure procedure. High frequency pressure waves in the fluid domain are avoided thanks to the gain in accuracy on the pressure loads. Here again the last two formulations provide very similar results.

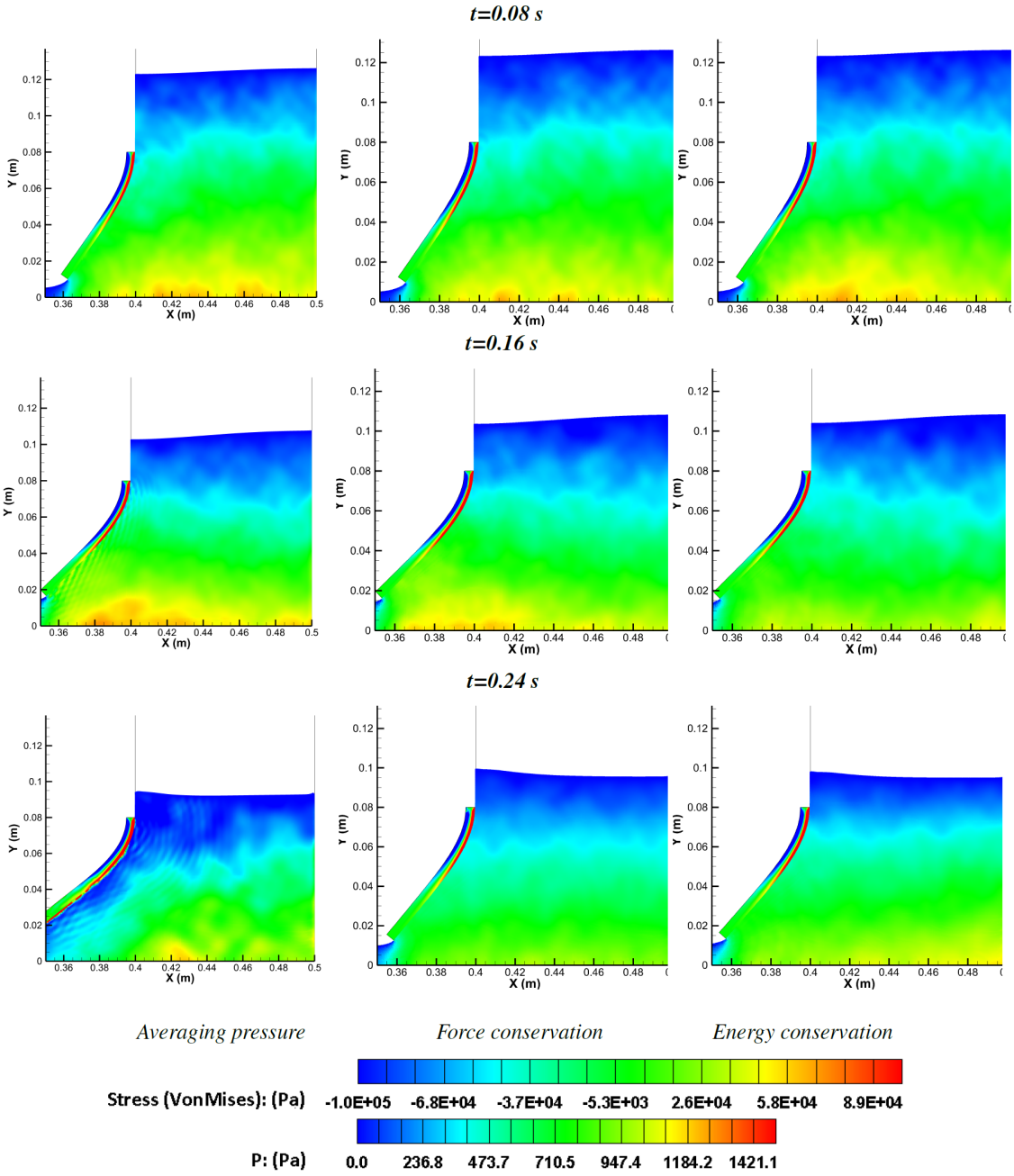

Fig. 39. Pressure field comparison for different load formulations (columns) at different instants (lines), HHT scheme with $\alpha_s = -0.05$.

6. Conclusion

The analysis of a SPH-FE coupling method has been provided from an energetic point of view with emphasis on interface coupling energy. An energy balance study has been proposed for both δ-SPH and Riemann-SPH schemes, highlighting the presence of a term representing the amount of energy dissipated or created at the fluid-structure interface. Inaccurate fluid loading leads to an accumulation of energy errors which are responsible for coupling instabilities. In this paper two different fluid loading procedures have been proposed to increase the conservation property of the coupling. The energy errors have been decreased and the robustness properties of the coupling have been improved. Only small differences were observed between the force and energy conservative formulations proposed.

However the energy conservative procedure requires the energy term calculation for all particles, slightly increasing the computational costs, so that the force conservative formulation could be preferred regarding the compromise between coupling accuracy, robustness and CPU time. Furthermore the proposed coupling method is relatively easy to implement and can be used with any kind of SPH or FE method.

References

[1] C. Antoci. Simulazione numerica dell´interazione fluidostruttura con la tecnica SPH. PhD thesis, University of Pavia, 2006.

[2] C. Antoci, M. Gallati, and Sibilla. S. Numerical simulation of fluid structure interaction by SPH. IOP Computers and Structures, 85:879–890, 2007.

[3] M. Antuono, A. Colagrossi, and S. Marrone. Numerical diffusive terms in weakly-compressible SPH scheme. Computer Physics Communications, 183:2570–2580, 2012.

[4] M. Antuono, S. Marrone, A. Colagrossi, and B. Bouscasse. Energy balance in the δ-SPH scheme. Computer Methods in Applied Mechanics and Engineering, 289:209–226, 2015.

[5] S.W. Attaway, M.W. Heinstein, and J.W. Swegle. Coupling of Smooth Particle Hydrodynamics with the Finite Element method. Nuclear Engineering and Design, 150:199–205, 1994.

[6] K.J. Bathe. Finite Element procedures. Prentice Hall, 1st edition, 1995.

[7] B. Bouscasse, A. Colagrossi, S. Marrone, and M. Antuono. Nonlinear water wave interaction with floating bodies in SPH. Journal of Fluids and Structures, 42:112–129, 2013.

[8] F. Caleyron, Y. Chuzel-Marmot, and A. Combescure. Modeling of reinforced concrete trough SPH-FE coupling and its application to the simulation of a projectile's impact onto a slab. i. International Journal for Numerical Methods in Biomedical Engineering, 27:882–898, 2009.

[9] J.L. Cercos-Pita, M. Antuono, A. Colagrossi, and A. Souto-Iglesias. Sph energy conservation for fluid-solid interactions. Computer Methods in Applied Mechanics and Engineering, 317:771–791, 2017.

[10] A. Colagrossi and A. Landrini. Numerical simulation of interfacial flows by smoothed particle hydrodynamics. Journal of Computational Physics, 191:448–475, 2003.

[11] M. De Leffe. Modelisation d ecoulements visqueux par methode SPH en vue d application a l hydrodynamique navale. PhD thesis, Ecole Centrale Nantes, 2009.

[12] T. De Vuyst, R. Vignjevic, and J.C. Campbell. Coupling between meshless and Finite Element methods. International Journal of Impact Engineering, 31:1054–1064, 2005.

[13] J. Degroote, P. Bruggeman, R. Haelterman, and Vierendeels J. Stability of a coupling technique for partitioned solvers in FSI applications. Computers & Structures, 86:2224–2234, 2008.

[14] M. Doring. Developpement d une methode SPH pour les applications a surface libre en hydrodynamique. PhD thesis, Ecole Centrale Nantes, 2005.

[15] C. Farhat and M. Lesoinne. Two efficient staggered algorithms for the serial and parallel solution of three dimensional nonlinear transient aeroelastic problems. Computer Methods in Applied Mechanics and Engineering, 182:499–515, 2000.

[16] G. Fourey. Developpement d une methode de couplage fluide structure SPH Elements Finis en vue de son application a l hydrodynamique navale. PhD thesis, Ecole Centrale Nantes, 2012.

[17] G. Fourey, C. Hermange, G. Oger, and D. Le Touzé. An efficient FSI coupling strategy between smoothed particle hydrodynamics and finite element methods. Computer Physics Communications, 217:66–81, 2017.

[18] R.A. Gingold and J.J. Monaghan. Smoothed Particle Hydrodynamics: theory and application to non-spherical stars. Monthly Notices of the Royal Astronomical Society, 181:375–389, 1977.

[19] P. Groenenboom and B. Cartwright. Hydrodynamics and fluid-structure interaction by coupled SPH-FE method. Journal of Hydraulic Research, 48:61–73, 2010.

[20] H.M. Hilber, T.J.R. Hughes, and R.L. Taylor. Improved numerical dissipation for time integration algorithms in structural dynamics. Earthquake Engineering and Structural Dynamics, 5(3):283–292, 1977.

[21] G. Johnson. Linking of lagrangian particle methods to standard finite element methods for high velocity impact computations. Nuclear Engineering and Design, 150:265–274, 1994.

[22] J. Leduc, F. Leboeuf, and M. Lance. Improvement of multiphase model using preconditioned riemann solvers. In Proceeding of the 5th international SPHERIC workshop, 2010.

[23] Z. Li. Développement d´une méthode de simulation de couplage fluide structure á láide de la méthode SPH. PhD thesis, Ecole Centrale Lyon, 2013.

[24] Z. Li, A. Combescure, and F. Leboeuf. Coupling of finite volume and finite element subdomains using different time integrators. International Journal For Numerical Methods in Fluids, 72:1286–1306, 2013.

[25] Z. Li, J. Leduc, J. Nunez-Ramirez, A. Combescure, and J-C. Marongiu. A non-intrusive partitioned approach to couple smoothed particle hydrodynamics and finite element methods for transient fluid-structure interaction problems with large interface motion. Computational Mechanics, 55(4):697–718, 2015.

[26] L. Libersky, A. Petschek, T. Carney, J. Hipp, and F. Allahdadi. High Strain Lagrangian Hydrodynamics: A three-dimensional SPH code for dynamic material response. Journal of Computational Physics, 109:67–75, 1993.

[27] T. Long, D. Hu, D. Wan, C. Zhuang, and G. Yang. An arbitrary boundary with ghost particles incorporated in coupled FEM-SPH model for FSI problems. Journal of Computational Physics, 350:66–183, 2017.

[28] L.B. Lucy. A numerical approach to the testing of the fission hypothesis. Astronomical Journal, 82:1013–1024, 1977.

[29] J-C. Marongiu. Méthode numérique lagrangienne pour la simulation d´ecoulements á surface libre. Application aux turbines Pelton. PhD thesis, Ecole Centrale Lyon, 2007.

[30] J-C. Marongiu, F. Leboeuf, J. Caro, and A. Parkison. Free surface flows simulations in Pelton turbines using an hybrid SPH-ALE method. Journal of Hydraulic Research, 48:40–49, 2010.

[31] S. Marrone, A. Colagrossi, A. Antuono, C. Lugni, and M.P. Tulin. A 2D+t SPH model to study the breaking wave pattern generated by fast ships. Journal of Fluids and Structures, pages 1199–1215, 2011.
[32] C. Michler, S.J. Hulshoff, E.H. Van Brummelen, and R. De Borst. A monolithic approach to fluid-structure interaction. Computers & Fluids, 33:839–848, 2004.
[33] J. Nunez-Ramirez, J-C. Marongiu, M. Brun, and A. Combescure. A partitioned approach for the coupling of sph and fe methods for transient nonlinear fsi problems with incompatible time-steps. International Journal for Numerical Methods in Engineering, 2016.
[34] G. Oger. Aspects theorique de la methode SPH et applications a l hydrodynamique a surface libre. PhD thesis, Ecole Centrale Nantes, 2006.
[35] G. Oger, M. Doring, B. Alessandrini, and P. Ferrant. Two-dimensional SPH simulations of wedge water entries. Journal of Computational Physics, 213:803–822, 2006.
[36] G. Oger, D. Le Touzé, D. Guibert, M. de Leffe, J. Biddiscombe, J. Soumagne, and J.-G. Piccinali. On distributed memory MPI-based parallelization of SPH codes in massive HPC context. Computer Physics Communications, 200:1–14, 2016.
[37] G. Oger, S. Marrone, D. Le Touzé, and M. De Leffe. Sph accuracy improvement through the combination of a quasi-Lagrangian shifting transport velocity and consistent ALE formalisms. Journal of Computational Physics, 313:76–98, 2016.
[38] S. Piperno. Simulation numérique de phénomènes dinteraction fluide structure. PhD thesis, Ecole Nationale des Ponts et Chaussees, 1995.
[39] S. Piperno and C. Farhat. Partitioned procedures for the transient solution of coupled aerobatic problems : Part II energy transfer analysis and three dimensional applications. Computer Methods in Applied Mechanics and Engineering, 190:3147–3170, 2001.
[40] P.W. Randle and L.D. Libersky. Smoothed particle hydrodynamics: Some recent improvements and applications. Computer methods in applied mechanics and engineering, 139:375–408, 1996.
[41] Y.M. Scolan. Hydroelastic behaviour of a conical shell impacting on a quiescentfree surface of an incompressible liquid. Journal of Sound and Vibration, 277:163–203, 2003.
[42] J.P. Vila. On particle weighted methods and smooth particle hydrodynamics. Mathematical Models and Methods in Applied Science, 9(2), 1999.
[43] H. Wendland. Piecewise polynomial, positive definite and compactly supported radial function of minimal degree. Advances in Computational Mathematics, 4:389–396, 1995.
[44] Q. Yang. SPH Simulation of Fluid Structure Interaction Problems with Application to Hovercraft. PhD thesis, Faculty of the Virginia Polytechnic Institute and State University, 2012.
[45] Q. Yang, V. Jones, and L. McCue. Free-surface flow interactions with deformable structures using an sphfem model. Ocean Engineering, 55:136–147, 2012.
[46] Z. Zhang, H. Qiang, and W. Gao. Coupling of smoothed particle hydrodynamics and finite element method for impact dynamics simulatio. Engineering Structures, 33:255–264, 2011.